Data-driven multi-objective inverse design of programmable Vorochiral metamaterials for customized orthotic midsoles

Hao Wang[a,b], Yuanfei Ren[c], Mohammed Rafiq Abdul Kadir[d], Hanxing Zhu[b], Yongtao Lyu[a,e,f,*]

[a] Department of Engineering Mechanics, School of Mechanics and Aerospace Engineering, Dalian University of Technology, No. 2 Linggong Road, Dalian, 116024, China

[b] School of Engineering, Cardiff University, Cardiff, UK

[c] The first Department of Hand and Foot Surgery, Central Hospital of Dalian University of Technology, Dalian, China

[d] Department of Biomedical Engineering, Faculty of Engineering, Universiti Malaya, Kuala Lumpur, 50603, Malaysia

[e] State Key Laboratory of Structural Analysis, Optimization and CAE Software for Industrial Equipment, Dalian University of Technology, Dalian, 116024, China

[f] Department of Engineering Mechanics, DUT-BSU Joint Institute, Dalian University of Technology, Dalian, 116024, China

[*] Correspondence to: Department of Engineering Mechanics, Dalian University of Technology, No. 2 Linggong Road, Dalian 116024, China. E-mail address: yongtaolu@dlut.edu.cn (Y. Lyu).

Keywords: Data-driven, Multi-objective inverse design, Deep learning, Genetic algorithm, Mechanical metamaterials, Orthotic midsoles

ABSTRACT

The customized design of advanced load-bearing components, such as foot orthoses, remains a critical engineering challenge due to the highly nonlinear relationships between architected metamaterial configurations and macroscopic mechanical performance. In this study, a data-driven multi-objective inverse design framework was proposed to optimize programmable Vorochiral mechanical metamaterials for customized orthotic midsoles. Guided by plantar pressure distributions, an infilling design strategy for plantar biomechanical modulation was implemented across the forefoot, midfoot, and heel regions to precisely mitigate high-pressure concentrations. Optimal Latin hypercube sampling and a variational autoencoder were employed to construct and augment the dataset, enabling the training of a robust backpropagation neural network (BPNN) surrogate model for efficient performance prediction under limited sample conditions. By integrating the BPNN with the non-dominated sorting genetic algorithm II, the Pareto front was efficiently extracted, and the optimal configuration parameters were identified using a comprehensive decision-making framework based on the entropy weight-TOPSIS method. The designed Vorochiral orthotic midsole was systematically evaluated through finite element simulations, mechanical experiments, as well as static standing and dynamic gait tests. The results demonstrated that, compared with midsoles infilled with conventional structures, the optimized Vorochiral midsole significantly reduced both peak and mean plantar pressures, achieving reductions of up to 33.24% and 37.94%, respectively. These findings highlight its strong potential for customized biomechanical interventions. Furthermore, the proposed framework establishes a generalizable data-driven paradigm for inverse design and performance modulation of architected metamaterials, facilitating efficient customized engineering design across broader application domains.

1. Introduction

Diabetic peripheral neuropathy and peripheral arterial disease are the predominant precursors to diabetic foot ulcers (DFUs), a severe complication that markedly increases the risk of lower-extremity amputation and patient mortality [1–6]. Extensive biomechanical studies have demonstrated that abnormal plantar pressure distribution, particularly elevated peak plantar pressure and localized shear stress, serves as the primary mechanical driver of soft tissue breakdown and ulceration in the diabetic foot [5–16]. Consequently, redistributing plantar pressure through accommodative foot orthosis, such as pressure-relieving insoles and customized cushioning midsoles, remains a key and challenging strategy for the conservative treatment and pro phylactic management of DFUs [17–27].

Mechanical metamaterials enable the precise tailoring of macroscopic mechanical properties, such as stiffness, Poisson's ratio, and energy absorption, through rational microstructural design [28–

40], positioning them as promising alternatives to conventional solid insoles and midsoles. Ning et al. [41] proposed a novel re-entrant insole and conducted a study involving 23 patients with diabetes. The results demonstrated that the insole effectively distributed plantar pressure and increased the contact area, thereby providing enhanced plantar offloading and cushioning. Cracknell et al. [19] developed a custom Gyroid-based orthotic insole using an optimization algorithm, demonstrating that the Gyroid insole reduced peak pressure by 12.2 kPa compared with a traditional insole and 94.3 kPa compared to barefoot condition.

Given that midsoles are thicker than insoles and more amenable to infill, considerable research has focused on midsole structures. Cheng et al. [17] investigated a three-dimensional (3D) Voronoi strut midsole, demonstrating excellent energy absorption and cushioning performance. Alam and Kwok [24] designed high-performance lattice midsole structures using a multidisciplinary optimization approach. Sun et al. [20] presented 3D-printed midsoles engineered with auxetic chiral metamaterials. Through a systematic parametric investigation of unit cell size, wall thickness, and nodal circle radius, an optimized structural configuration was identified, showing significant improvements in both biomechanical response and user comfort. Currently, a novel class of random chiral structures, termed Vorochiral metamaterials, was proposed by integrating Voronoi tessellation with chiral architectures [42]. The Vorochiral structure exhibits inherent advantages in stiffness and energy absorption due to its unique topological configuration and deformation mechanisms. Therefore, Vorochiral metamaterials with programmable mechanical properties have strong potential to infill structures for midsoles, enabling effective plantar offloading and cushioning when coupled with appropriate optimization strategies. Additionally, due to the complexity of the Vorochiral structure, additive manufacturing is the only feasible method for its realization.

Despite the significant potential of Vorochiral structures, their practical engineering design for diabetic midsoles presents a challenging and mutually conflicting multi-objective problem: minimizing the apparent Young's modulus (E), an indicator of stiffness, while simultaneously maximizing specific energy absorption (SEA). For vulnerable diabetic feet, high-risk regions require the lowest possible local stiffness to maximize contact area, thereby mitigating peak pressures that contribute to ulcer formation at their source [43–45]. Conversely, excessively low stiffness may lead to premature "bottoming-out" under dynamic walking loads, resulting in a critical loss of cushioning capacity [17,41,46]. Therefore, under the constraint of minimal stiffness, the structure must simultaneously exhibit high efficiency, lightweight characteristics, and superior energy absorption performance (i.e., high SEA). In conventional solid mechanics, stiffness and energy absorption are typically positively correlated, making this requirement inherently conflicting. Resolving this trade-off to identify an optimal balance remains a key challenge in the customized design of high-performance midsoles.

To address the inherent trade-offs in structural properties, the multi- objective inverse design paradigm has been widely adopted. Conventional approaches based on "trial-and-error" forward design or pure finite element (FE) analysis are computationally prohibitive for resolving such multi-objective conflicts. In contrast, multi-objective in verse optimization design enables efficient exploration of the design space to identify optimal solutions. Recent studies have demonstrated that competing objectives, such as stiffness and SEA in chiral, Voronoi, and biomimetic metamaterials, can be effectively balanced through multi-objective optimization [47–49]. However, the exploration of complex geometries remains fundamentally limited by the high computational cost of forward simulations, To overcome this limitation, the data-driven inverse design frameworks have been increasingly employed, in which metamaterial architectures are directly recon structed from target macroscopic responses using machine learning models [50–52]. By integrating these approaches, a multi-objective in verse optimization design framework can be established. Within this framework, computationally expensive FE analyses are replaced by high-fidelity surrogate models, enabling rapid extraction of the Pareto front for customized stiffness and enhanced energy absorption [53–59]. This approach ensures that the complex biomechanical requirements of customized midsoles can be efficiently fulfilled.

In this study, a data-driven multi-objective inverse design framework integrating data augmentation, surrogate modeling, evolutionary optimization, and decision-making was proposed to develop customized orthotic midsoles based on programmable Vorochiral mechanical metamaterials. Guided by plantar pressure distributions, an infilling design strategy was implemented across the forefoot, midfoot, and heel regions to mitigate high-pressure concentrations. Optimal Latin hypercube sampling (OLHS) and a variational autoencoder (VAE) were employed to construct and augment the dataset to overcome the problem of small samples, enabling the training of a highly accurate backpropagation neural network (BPNN) surrogate model. By integrating this surrogate model with the non-dominated sorting genetic algorithm II (NSGA-II) and a comprehensive decision-making framework based on the entropy weight-TOPSIS method, optimal structural configuration was efficiently identified from the Pareto front. Through comprehensive FE simulations, mechanical testing, as well as static standing and dynamic gait experiments, the optimized Vorochiral midsole was demonstrated to exhibit significantly lower peak and mean plantar pressures compared with midsoles infilled with conventional structures, highlighting its strong potential for customized biomechanical interventions. Furthermore, the proposed framework establishes a generalizable data-driven paradigm for inverse design and performance modulation of architected metamaterials, facilitating efficient customized engineering design across broader application domains.

2. Methods

This section describes the design methodology, FE analysis, mechanical experiments, and measurements under static standing and dynamic gait conditions. First, a partitioning and infilling strategy for the midsole is proposed, and a multi-objective inverse optimization framework is employed to determine the optimal configuration parameters of the Vorochiral metamaterial. Second, FE simulations and experimental tests are conducted to validate the accuracy of the predicted model. Finally, the optimized midsole is evaluated under static standing and dynamic gait conditions.

The data-driven workflow integrating BPNN with NSGA-II is shown in Fig. 1. First, the dataset with the design parameters and mechanical properties of Vorochiral metamaterials was augmented using VAE to overcome the problem of small samples, followed by forward prediction based on BPNN. Second, the well-trained BPNN surrogate model was incorporated into NSGA-II to inversely design the desirable structures.

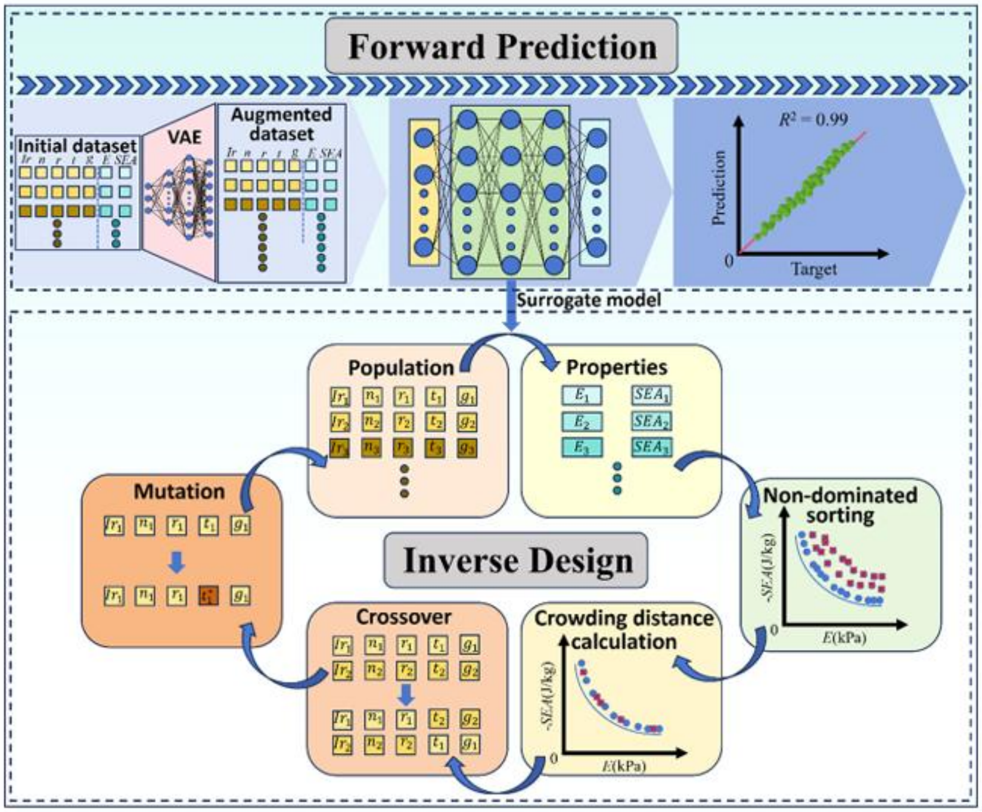

Fig. 1. Workflow of data-driven multi-objective inverse design.

2.1. Partitioning strategy of the midsole

The midsole was partitioned into several regions according to the distribution of plantar pressure. Previous studies have adopted partitioning strategies for midsole design [17,60,61]. In the present study, the midsole was primarily divided into three regions for structural infilling. To characterize the pressure distribution in each region, plantar pressure data were acquired using a Pedar-X pressure measurement system (Novel GmbH, Munich, Germany) during static standing, as shown in Fig. 2(a). A healthy male subject (weight: 78.9 kg, height: 178.6 cm, and foot length: 253.5 mm) participated in the measurement. The subject had no history of foot injury or disease within the past year. Two-dimensional (2D) and 3D plantar pressure distribution maps were obtained, as shown in Figs. 2(b) and 2(c). The higher plantar pressures are concentrated in the forefoot and heel regions, consistent with the biomechanical characteristics of the human foot. These findings confirmed the presence of two primary high-pressure regions. Accordingly, the midsole was divided into three sections, namely forefoot, midfoot, and heel, as shown in Fig. 2(d). Additionally, the tip of the sole typically does not come into contact with the foot. The total length of the midsole designed in this study was 255.0 mm, with the forefoot and heel sections each measuring 90.0 mm and the midfoot section measuring 60.0 mm. These dimensions were designed to facilitate infilling. To mitigate concentrated plantar pressure, the design focuses primarily on forefoot and heel regions, as highlighted by the solid red boxes of Fig. 2 (d).

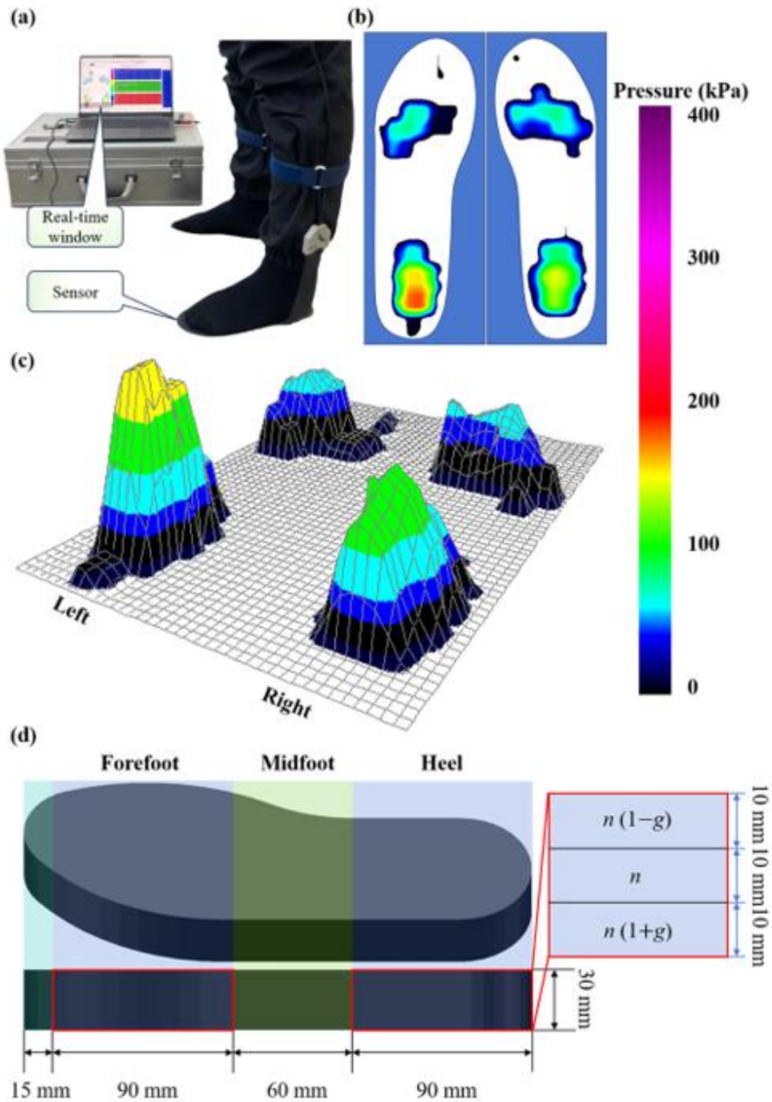

Fig. 2. Partitioning of the midsole based on plantar pressure distributions. (a) Measurement of plantar pressure distribution. (b) 2D plantar pressure map. (c) 3D plantar pressure map. (d) Midsole partitioning strategy. The solid red boxes indicate the forefoot and heel regions, which are further divided into upper, middle, and lower sections.

It should be noted that the optimized Vorochiral midsole fabricated for experimental validation represents a generalized "one-size-fits-most" high-performance prototype, rather than a design custom-tailored to subject A's specific plantar pressure map. The inclusion of subject A in the testing served exclusively as a methodological demonstrator. By stand-testing subject A on the ground, the aim is to prove the reliability of the proposed macroscopic layout strategy. Specifically, dividing the human plantar area into distinct functional regions (forefoot, midfoot, and heel) and infilling these regions with gradient Vorochiral configurations is a viable approach to mitigate local stress concentrations.

2.2. Infilling strategy of the midsole

Vorochiral metamaterials, as reported in our previous work, were employed as infilling structures for the midsole in this study due to their excellent mechanical properties [42]. To determine the optimal configuration of Vorochiral metamaterials, BPNN and NSGA-II were utilized. Additionally, OLHS was adopted to reduce computational costs, while data augmentation based on VAE was implemented to expand the dataset for improving the accuracy of prediction.

2.2.1. Optimal Latin hypercube sampling

The Vorochiral metamaterials were generated by integrating Vor onoi architectures with chiral structures, thereby introducing chirality into the Voronoi framework. These metamaterials were first proposed in our previous study [42], and have demonstrated excellent mechanical properties. Based on randomly distributed seed points, Vorochiral diagrams were constructed using MATLAB (v2023b, MathWorks Inc., Massachusetts, USA). The degree of irregularity was first defined by Zhu et al. [62,63]. For a regular hexagonal honeycomb with n cells in a square area A_0, the distance α_0 between any two adjacent nuclei is constant and given as:

$$\alpha_0 = \sqrt{\frac{2A_0}{n\sqrt{3}}} \tag{1}$$

For a random Voronoi diagram with n cells in the square area A_0, the irregularity degree Ir of the Voronoi tessellation is defined as:

$$Ir = 1 - \frac{\alpha}{\alpha_0} \tag{2}$$

where α denotes the minimum distance between any two nuclei [62,63]. The vertices of the Voronoi tessellation were replaced by nodal circles of equal radius, with tangentially connected ligaments linking adjacent nodal circles, as shown in Fig. 3(a). To generate the Vorochiral diagram, each vertex was traversed using an adjacency matrix. If two adjacent circles intersected or were tangent to each other, no connecting ligaments were generated to avoid geometric overlap. For instance, two trichiral metamaterials can be merged into a tetrachiral metamaterial, as shown in Fig. 3(a). Therefore, the Vorochiral metamaterial represents a combination of multiple chiral configurations. Fully defined by the radius of nodal circles r and wall thickness t, the geometric models of the Vorochiral metamaterials were constructed using SolidWorks (v2023, SolidWorks inc., Massachusetts, USA), as shown in Fig. 3(b). For infilling the forefoot and heel regions of the midsole, the design domain A_0 was defined as an area of 90.0×30.0 mm^2, as shown in Fig. 3(b).

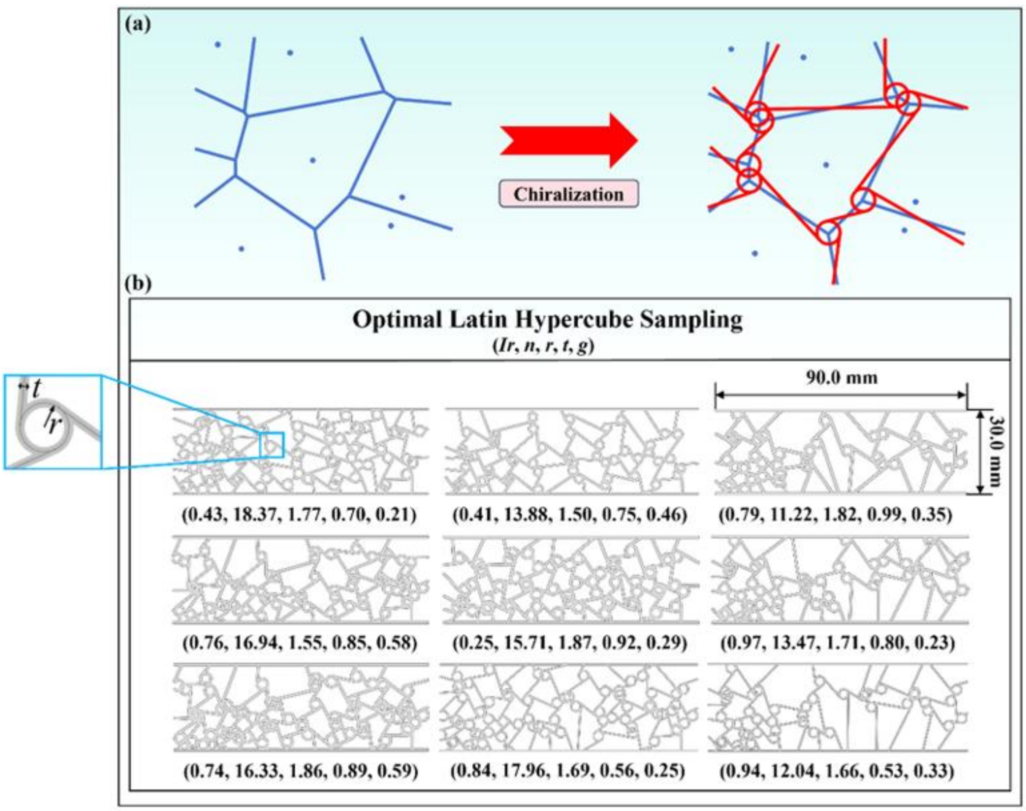

Fig. 3. Generation process and representative configurations of Vorochiral metamaterials via optimal Latin hypercube sampling (OLHS). (a) Chiralization process of Vorochiral metamaterials. (b) Representative configurations generated by OLHS (all configurations are provided in Supplementary Figure 1).

To reduce computational cost, OLHS was employed in this study. Five key design variables of the Vorochiral metamaterials were considered, namely *Ir, n, r, t,* and gradient factor *g*, all of which influence the mechanical properties of the structures. The gradient factor g governed the spatial distribution of seed points in the Vorochiral metamaterials, as shown in Fig. 2(d). The forefoot and heel regions of the midsole were divided into three equal sections, i.e., upper, middle, and lower sections. The number of seed points in these sections was defined as $n(1-g)$, n, and $n(1+g)$, respectively. The ranges of these design variables were determined based on the geometric constraints of the midsole and manufacturing considerations. Accordingly, the ranges of *Ir, n, r, t*, and *g* were set to 0.2–1.0, 10.0–20.0, 1.5–2.0, 0.5–1.0, and 0.2–0.6, respectively. Using OLHS, fifty distinct configurations of Vorochiral meta materials were generated. Representative configurations are shown in Fig. 3(b), while the complete set of configurations is provided in Supplementary Figure 1.

The design variables Ir, n, r and t were adopted from our previous study, where their geometric meanings and influences on the effective stiffness and energy absorption performance of Vorochiral meta materials were systematically investigated [42]. Briefly, these parameters govern the degree of structural irregularity, cellular topology, ligament geometry, and relative density, thereby determining the macroscopic mechanical response. Furthermore, a gradient factor g was introduced in the present study to characterize the spatial variation of the cellular architecture, enabling the inverse design of functionally graded orthotic midsoles with region-specific mechanical properties.

2.2.2. Calculation of the structural mechanical properties

The E and SEA were employed to evaluate the mechanical performance of the midsole. In patients with diabetic foot, plantar soft tissues are highly vulnerable and are often accompanied by sensory loss due to neuropathy. Therefore, it is essential to minimize the local stiffness of the midsole to ensure sufficient compliance, thereby maximizing the plantar contact area and effectively reducing peak plantar pressure. Accordingly, E was selected as a key evaluation metric in the midsole design. During walking, particularly in the heel-strike phase, the foot is subjected to continuous impact from ground reaction forces. To protect foot joints and soft tissues, the midsole must exhibit high energy ab sorption capability. Consequently, SEA was considered as another key evaluation metric. To determine the values of E and SEA for these fifty Vorochiral metamaterials, FE analysis was performed using Abaqus (v2021, Dassault SIMULIA, Rhode Island, USA). The material properties of the thermoplastic polyurethane (TPU) used for fabricating the mid soles were experimentally characterized to ensure accurate FE simulations.

Dumbbell-shaped standard tensile specimens were fabricated using the fused deposition modeling (FDM) technique with a Bambu Lab P1S 3D printer (Shenzhen, China), as shown in Fig. 4(a). A nozzle diameter of 0.4mm was used, with a printing speed of 40.0mm/s and a fixed layer height of 0.08mm. TPU 95A HF, supplied by Bambu Lab, was utilized as the base materials for specimen fabrication.

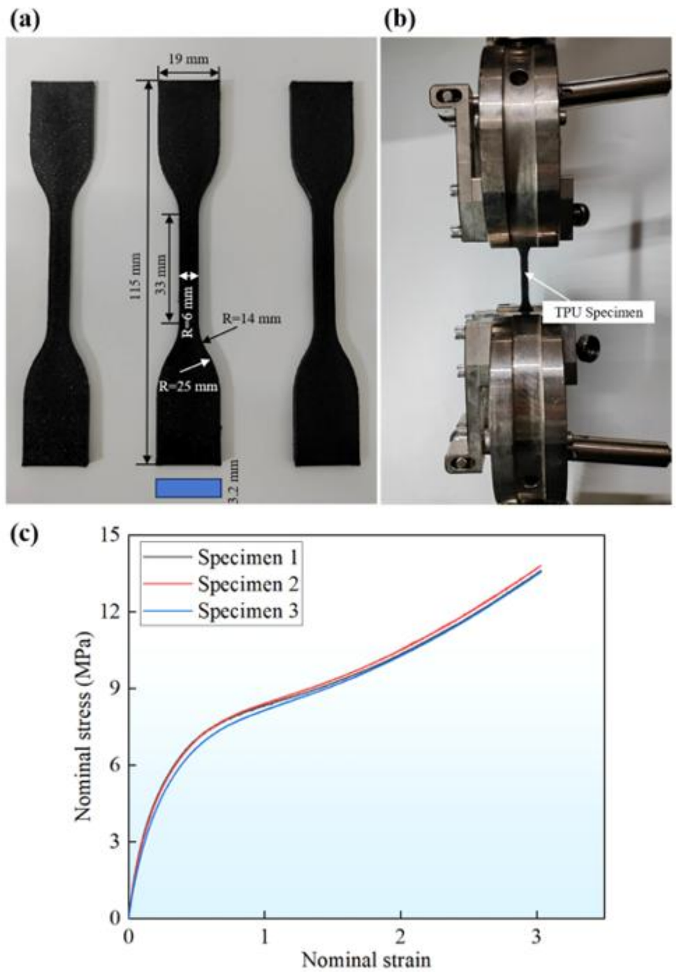

Fig. 4. Specimens and experimental setup. (a) Standard dumbbell-shaped TPU tensile specimens and their dimensions. (b) Uniaxial tensile testing setup. (c) Nominal stress-strain curves of the TPU materials.

The mechanical properties of TPU were determined through uniaxial tensile testing. According to the ASTM D638 international standard, three dumbbell-shaped TPU specimens were designed and fabricated. The specimen geometry and dimensions are shown in Fig. 4(a). The tests were conducted using a universal testing machine (MTS Criterion 43.104) with a load capacity range of 10.0–10.0kN and a maximum force measurement error of less than ±1.0%. A constant loading speed of 10.0mm/min was applied in all tests, as shown in Fig. 4(b). During loading, force-displacement data were recorded and subsequently con verted into nominal stress-strain curves. Based on the obtained stress- strain data, constitutive fitting was performed to characterize the hyperelastic behavior of TPU using Abaqus 2021. Several hyperelastic constitutive models, including Arruda-Boyce, Yeoh, Mooney-Rivlin, Ogden, Neo-Hookean, and Polynomial models, were evaluated against the average nominal stress-strain response. Among these, the second- order Polynomial model (N=2) provided the best fit. The three experimentally obtained nominal stress-strain curves are shown in Fig. 4 (c). The fitted material parameters of the Polynomial hyperelastic model are summarized in Table 1and were subsequently used to define the TPU material properties in the FE simulations.

Table 1
Material parameters of TPU.

ρ (g/cm^3)	C_{10}	C_{01}	C_{20}	C_{02}	C_{11}	D_1	D_2
1.22	− 8.95	15.95	0.10	3.30	− 0.51	0.00	0.00

FE simulations were performed using the commercial software Abaqus/Explicit 2021. The second-order Polynomial (N=2) hyperelastic constitutive model was employed to represent the mechanical behavior of the metamaterials. Two rigid plates were positioned above and below the Vorochiral metamaterial, as shown in Fig. 5(a). The metamaterial was discretized using eight-node reduced-integration hexahedral solid elements (C3D8R), while the rigid plates were modeled using quadrilateral rigid shell elements (R3D4). A mesh size of 0.36mm was based on a mesh convergence analysis. The bottom rigid plate was fully constrained, whereas a downward displacement of 20.0mm was applied the top rigid plate to compress the metamaterial. All nodes of the top and bottom plates were coupled to their respective reference points, and the boundary conditions and loading, as shown in Fig. 5(a), were applied to these reference points. A friction coefficient of 0.2 was defined for the tangential contact between the rigid plates and the metamaterial, while hard contact was specified for the normal interaction. The force-displacement response was obtained by extracting the reaction forces and displacements of the top reference point. Subsequently, the corresponding stress-strain curves were derived to evaluate the mechanical performance of the Vorochiral metamaterials.

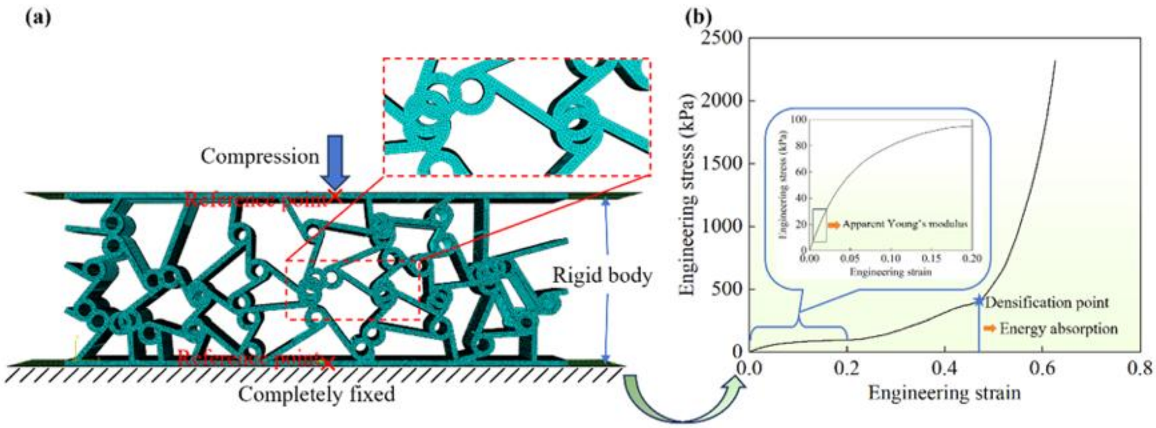

Fig. 5. FE model and engineering stress-stain response of the Vorochiral metamaterial. (a) FE model. Two rigid plates are positioned at the top and bottom of the structure. The blue arrow indicates the compressive direction, and the red dashed box highlights a magnified mesh region. (b) Apparent Young's modulus (E) and energy absorption (EA) derived from the compressive stress-strain curve. The inset shows a magnified view, and the blue star indicates the densification point.

E is an indicator of stiffness, reflecting the ability of a structure to resist deformation. It is determined from the linear elastic region of the engineering stress-strain curve, as shown in Fig. 5(b). The value of E is calculated as:

$$E = \frac{F/A}{\Delta h/H} \tag{3}$$

where *F* denotes the compressive load, *H* is the initial height of the structure, *A* and Δh are the area and displacement of upper surface of the structure, respectively.

SEA is an indicator of the energy absorption capacity per unit mass, which can be calculated as:

$$SEA = \frac{EA}{\rho_m \rho_v} \tag{4}$$

where *EA* is the energy absorption per unit volume, ρm denotes the density of the base material, and ρ_v represents the relative density of the structure. The parameter *EA* is obtained by integrating the stress-strain curve as shown in Fig. 4(b).

$$EA = \int_0^{\varepsilon_d} \sigma(\varepsilon)\mathrm{d}\varepsilon \tag{5}$$

where ε is the engineering strain, σ(ε)is the corresponding engineering stress, and ε_d denotes the strain at the densification point.

Accordingly, these two key mechanical properties were evaluated for the fifty Vorochiral metamaterial configurations generated using OLHS, forming an initial dataset of fifty training data for subsequent deep learning.

All configurations were designed with an out-of-plane thickness of 15.0mm to prevent buckling and global instability under quasi-static compression while improving computational efficiency. It should be emphasized that all design variables (*Ir, n, r, t* and **g**) are defined by the 2D cellular topology. In the customized orthotic midsole, the same cross- sectional architecture was extruded along the out-of-plane thickness direction according to the plantar profile, without introducing additional geometric design variables. Consequently, the dataset and the final 3D midsole share identical topological characteristics and loading orientation, enabling an efficient mapping from the surrogate model to the practical 3D structure.

2.2.3. Data augmentation via VAE

Since the initial dataset contained only fifty samples, it was necessary to expand the dataset to enable effective training of the predictive model. Therefore, a data augmentation approach based on VAE was adopted to generate a large amount of data required for model training.

The VAE is a neural network-based generative model that combines the concepts of variational inference and autoencoders. Its objective learning is to learn the latent probability distribution of the input data and to generate new samples by drawing from this distribution, thereby producing data that resemble the original dataset. In a VAE, the latent variable z is defined as a random variable following a predefined prior distribution, typically a standard multivariate Gaussian distribution:

$$p(z) \sim N \tag{6}$$

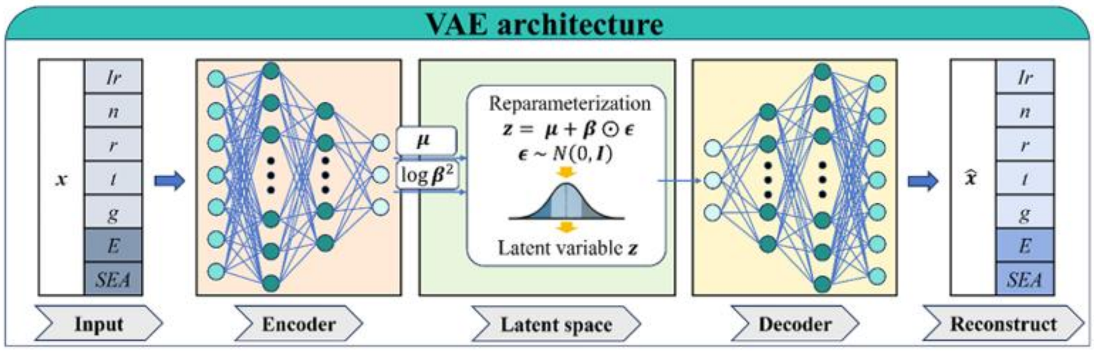

Fig. 6. Architecture of the VAE. The model consists of an encoder and a decoder, each with two hidden layers. The encoder contains 32 and 16 neurons in the first and second layers, respectively, while the decoder follows a mirrored structure. The latent dimension is set to 3. A reparameterization technique is employed to enable backpropagation.

The encoder learns an approximate posterior distribution $q_0(z|x)$, where x represents the design parameters of the structure and the associated mechanical properties, as shown in Fig. 6. The distribution is parameterized by a mean vector μ and a log-variance vector $\log\beta^2$. To enable backpropagation, a reparameterization technique is applied:

$$z = \mu + \beta \odot \epsilon, \quad \epsilon \sim N(0, I) \tag{7}$$

where ϵ denotes a noise term from the standard normal distribution $q_0(z|x)$. To ensure latent space regularization while optimizing both reconstruction and prediction performance, a combined loss function has been defined as:

$$L = L_{\text{recon}} + \gamma D_{\text{KL}}(q(z|x) \parallel p(z)) \tag{8}$$

where L is the total loss, L_{recon} denotes the reconstruction loss, D_{KL} represents the Kullback-Leibler (KL) divergence loss, and γ which is a weighting factor of the KL divergence term, set to 0.001 in this study. The L_{recon} and D_{KL} are given by:

$$L_{\text{recon}} = \frac{1}{N}\sum_{i=1}^{N} \|x_i - \hat{x}_i\|^2 \tag{9}$$

$$D_{\text{KL}} = -\frac{1}{2}\sum_{j=1}^{d}\left(1 + \log\beta_j^2 - \mu_j^2 - \beta_j^2\right) \tag{10}$$

where d denotes the latent dimension, which was set to 3 in this study. Both the encoder and decoder consisted of two hidden layers. In the encoder, the first and second hidden layers contained 32 and 16 neurons, respectively, whereas the decoder employed a mirrored architecture.

Using the proposed data augmentation approach, the dataset was initially expanded to 3000 samples. Samples falling outside the predefined parameter ranges were subsequently removed, resulting in a final dataset of 1800 samples. In total, 1750 new samples resembling the original data were generated. The dataset was then split into training, validation, and testing datasets with proportions of 70%, 15%, and 15%, respectively.

2.2.4. Forward prediction via BPNN

The BPNN is a classical in deep learning model that utilizes errors backpropagation to learn nonlinear mappings between inputs and outputs [64]. In this study, a nonlinear mapping relationship was established between the input vector x and the output vector y:

$$y = \text{BPNN}(x) = \text{BPNN}(Ir, n, \quad r, \quad t, \quad g) \tag{11}$$

where y denotes the predicted mechanical properties, namely *E* and *SEA*, of the Vorochiral metamaterials.

The architecture of the BPNN employed in this study is shown in Fig. 7(a). The input layer consists of five design parameters (*Ir, n, r, t*, and *g*), while the output layer contains two indicators of mechanical properties (*E* and *SEA*). The hidden layers are fully connected and positioned between the input and output layers, with each neuron connected to all neurons in adjacent layers. No intra-layer connections exist. The forward process of activation and signal propagation from input variables to output variables simulates the activity of neurons in the human brain. Each neuron is a nonlinear activation resulting from a linear combination of weights, biases, and the outputs of neurons in the previous layer, as shown in Fig. 7(b). Among common activation functions (ReLU, Tanh, and Sigmoid), the Sigmoid function was adopted in this study:

$$a_j^l = \frac{1}{1+e^{-x}}\left(\sum a_k^{l-1}\omega_{j,k}^l + b_j^l\right) \tag{12}$$

where a^l_j denotes the activation of the j$^{\text{th}}$ neuron in the l^{th} layer, $\omega^l_{j,k}$ represents the weight connecting the k^{th} neuron in the previous layer, and b^l_j is the bias term.

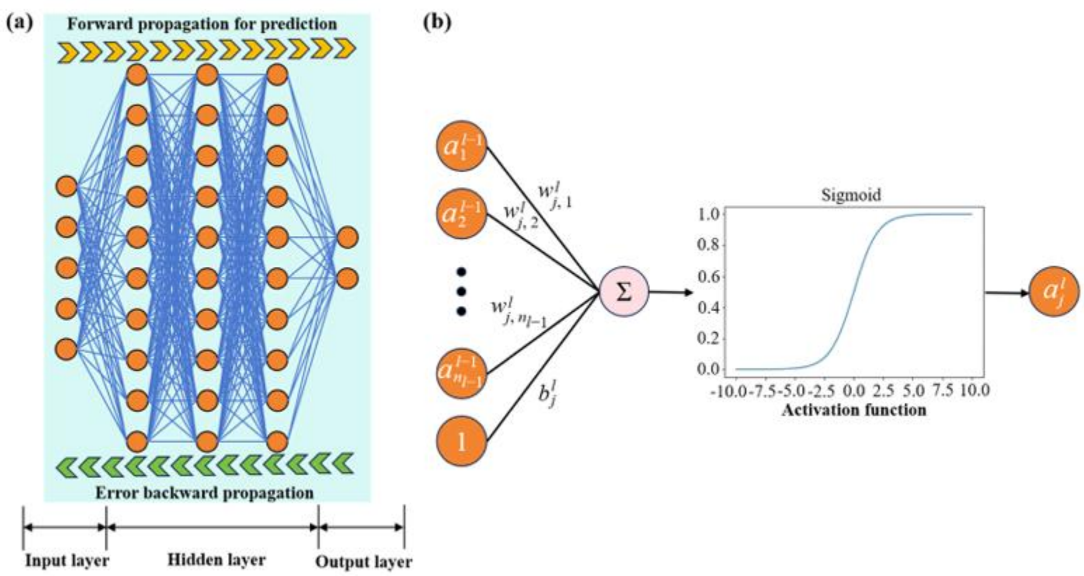

Fig. 7. Architecture of the BPNN model. (a) Structure of the BPNN, including input, hidden and output layers. (b) A neuron is the nonlinear activation of a linear combination of weights, biases and neurons from previous layer.

The prediction error between the model output h and the true value y was minimized through error backpropagation using the gradient descent theory. The mean squared error (MSE) was adopted as the loss function, which is widely used for regression tasks.

$$MSE = \frac{1}{m}\sum_{i=1}^{m}\|\boldsymbol{h}_i - \boldsymbol{y}_i\|^2 \tag{13}$$

where m is the number of samples, $\boldsymbol{h}_i$ is the predicted output of the i-th sample, and $\boldsymbol{y}_i$ is the corresponding ground truth. The notation $\|\cdot\|$ indicates the L^2 (Euclidean) norm. Additionally, the coefficient of determination (R_2) was used to evaluate the regression performance.

$$R^2 = 1 - \frac{\sum_{i=1}^{m} \|\boldsymbol{y}_i - \boldsymbol{h}_i\|^2}{\sum_{i=1}^{m} \|\boldsymbol{y}_i - \boldsymbol{o}_i\|^2} \tag{14}$$

where $\boldsymbol{o}_i$ denotes the average of real output.

The hyperparameters of the BPNN significantly influence prediction accuracy. Therefore, a hyperparameter sensitivity analysis was conducted to determine the optimal network architecture. The number of hidden layers was varied from one to four, while the number of neurons in each hidden layer was set to 6, 8, and 10. The network architecture was defined as follows: five neurons in the input layer, three hidden layers with 10 neurons each, and two neurons in the output layer. Furthermore, the network was trained using the Adam optimizer with an initial learning rate set to 0.001. This value was carefully selected to ensure a steady and computationally efficient convergence while preventing the loss function from oscillating near the global minimum. Such an optimal learning rate provided the necessary gradient resolution to accurately establish the complex, highly non-linear mappings between the metamaterial design space and the target mechanical properties [65, 66]

2.2.5. Multi-objective inverse optimization design

To navigate the complex Pareto-optimal design space, the well- trained BPNN surrogate model was integrated with the NSGA-II [67]. NSGA-II was specifically selected over other heuristic algorithms due to its robust non-dominated sorting mechanism, fast convergence rate, and proven superiority in maintaining population diversity for highly non-linear metamaterial design problems [67,68]. The overall workflow of the optimization process is illustrated in Fig. 8. The design variables of the Vorochiral metamaterials included the degrees of irregularity $Ir \in [0.2, 1.0]$, the number of seed points $n \in [10.0, 20.0]$, nodal circle radius $r \in [1.5, 2.0]$, wall thicknesses $t \in [0.5, 1.0]$, and gradient factors $g \in [0.2, 0.6]$. The optimization objectives were defined as minimizing E and maximizing SEA, as expressed in Eq. (15). Through iterative genetic operation including crossover, mutation, non-dominated sorting, and crowding distance calculation, the Pareto front was obtained and converged to a stable distribution. Multiple optimal solutions on the Pareto front were identified on the Pareto front, representing different trade-offs between stiffness and energy absorption. The extended entropy-weight TOPSIS method was subsequently applied to rank the

Pareto solutions and select the most representative design by comprehensively considering solution quality, stability, ranking consistency, and diversity. It should be noted that NSGA-II is responsible for exploring the Pareto-optimal solution set, whereas the extended entropy-weight TOPSIS method is only used for decision-making among the obtained Pareto solutions rather than performing the optimization itself.

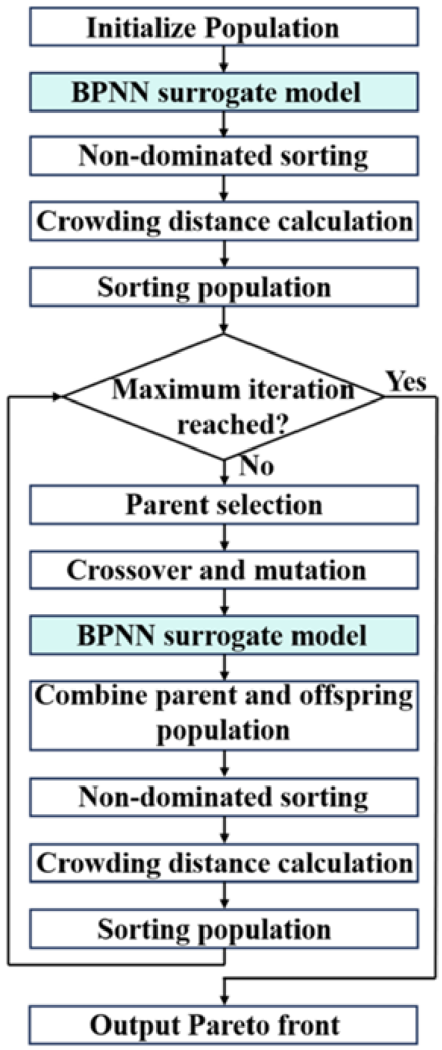

Fig. 8. Flow chart of the multi-objective inverse optimization design process. The BPNN surrogate model is integrated into the NSGA-II algorithm.

Although the E and SEA characterize different stages of the compressive response, they represent complementary mechanical requirements for orthotic midsoles. During walking, the cellular structure undergoes progressive compression under plantar loading rather than remaining exclusively within the linear elastic regime. A relatively low E contributes to improved cushioning and reduced peak plantar pressure during the initial loading stage, whereas a high SEA enhances impact attenuation as deformation increases. Therefore, simultaneously optimizing these two-performance metrics enables a balanced design that satisfies both comfort and energy absorption requirements.

$$\begin{cases} \min E(Ir, \quad n, \quad r, \quad t, g) \\ \max SEA(Ir, \quad n, \quad r, \quad t, g) \\ s.t. \begin{cases} 0.2 \le Ir \le 1.0 \\ 10.0 \le n \le 20.0 \\ 1.5 \le r \le 2.0 \\ 0.5 \le t \le 1.0 \\ 0.2 \le g \le 0.6 \end{cases} \end{cases} \tag{15}$$

To identify the knee point, a comprehensive decision-making framework based on the entropy weight-TPOSIS method which is a technique for order preference by similarity to ideal solution was employed [49,69,70]. The selected knee-point solution was regarded as the optimal inverse design result, and its corresponding design variables were adopted as the final structural parameters. The specific procedure is outlined as follows:

Step1: Constructing the Pareto front matrix

The Pareto front is defined as:

$$X = \begin{bmatrix} E_1 & SEA_1 \\ E_2 & SEA_2 \\ \vdots & \vdots \\ E_a & SEA_a \end{bmatrix} \tag{16}$$

where a denotes the number of solutions on the Pareto front.

Step 2: Normalization of objective functions

The objective functions are normalized. For E, where smaller values are preferable, a positive transformation is applied:

$$E_a^* = \frac{\max - E_a}{\max - \min} \tag{17}$$

For SEA, where larger values are preferable, the normalization is defined as:

$$SEA_a^* = \frac{SEA_a - \max}{\max - \min} \tag{18}$$

The normalized matrix is:

$$Y = \begin{bmatrix} E_1^* & SEA_1^* \\ E_2^* & SEA_2^* \\ \vdots & \vdots \\ E_a^* & SEA_a^* \end{bmatrix} \tag{19}$$

Step 3: Construction of the index weight p_{ij}

$$p_{ij} = \frac{y_{ij}}{\sum_{j=1}^{2} y_{ij}} \tag{20}$$

where y_{ij} denotes the j^{th} response of the i^{th} evaluation item in the normalized matrix Y, where i=1,2,…,a, j=1, 2 correspond to E and SEA, respectively.

Step 4: Calculation of the index entropy values e_j

$$e_j = -\frac{1}{\ln(a)} \sum_{j=1}^{2} p_{ij} \ln\left(p_{ij}\right) \tag{21}$$

Step 5: Determination of entropy weights w_j

$$d_j = 1 - e_j \tag{22}$$

$$w_j = \frac{d_j}{\sum_{j=1}^{2} d_j} \tag{23}$$

$$w_1 + w_2 = 1 \tag{24}$$

where d_j denotes the information utility value, and w_1 and w_2 represent the response weights of E and SEA, respectively.

Step 6: Construction of the weighted decision-making matrix

Multiplying the entropy weight values obtained in Step 5 with the normalized matrix to derive the weighted decision-making matrix by the entropy weight method

$$v_{ij} = w_j y_{ij} \tag{25}$$

Step 7: Determination of the positive ideal solution and negative ideal solution

The positive ideal solution v+ j is the minimum value of the evaluation indicators

$$v_j^+ = (\min v_{1j}, \quad \min v_{2j}, \ldots, \min v_{aj}) \tag{26}$$

The negative ideal solution v_j is the maximum value of the evaluation indicators

$$v_j^- = (\max v_{1j}, \quad \max v_{2j}, \ldots, \max v_{aj}) \tag{27}$$

Step 8: Calculation of Euclidean distance

The distance to the positive solution is

$$d_i^+ = \sqrt{\sum_{j=1}^{2} \left(v_{ij} - v_j^+\right)^2} \tag{28}$$

The distance to the negative solution is

$$d_i^- = \sqrt{\sum_{j=1}^{2} \left(v_{ij} - v_j^-\right)^2} \tag{29}$$

Step 9: Calculation of the closeness coefficient (TOPSIS Score)

$$C_i = \frac{d_i^-}{d_i^+ + d_i^-} \tag{30}$$

where the larger the C_i value, the closer it is to the ideal solution.

Step 10: Stability indicator S_i

The stability score S_i is defined as the selection frequency of each solution under multiple perturbations:

$$S_i = \frac{1}{N}\sum_{k=1}^{N}\delta(i_k = i) \quad (31)$$

where N denotes the total number of perturbations, i_k indicates the index of the best solution obtained in the kth run, and $\delta(\cdot)$ is the indicator function and defined as $\delta(true)$=1, and $\delta(false)$=0.

Step 11: Rank stability R_i

The rank stability R_i is calculated based on the normalized ranking position:

$$R_i = 1 - \frac{r_i - 1}{a - 1} \quad (32)$$

where r_i denotes the ranking position of the i^{th} solution based on the TOPSIS score.

Step 12: Diversity indicator D_i

The diversity score D_i is defined as the average Euclidean distance between each solution and all other solutions in the normalized objective space:

$$D_i = \frac{1}{n-1}\sum_{k\neq i} d_{ik} \quad (33)$$

$$d_{ik} = \sqrt{\sum_{j=1}^{2}\left(\widetilde{x}_{ij} - \widetilde{x}_{uj}\right)^2} \quad (34)$$

$$\widetilde{x}_{ij} = \frac{x_{ij} - x_j^{\min}}{x_j^{\max} - x_j^{\min}} \quad (35)$$

where d_{ik} denotes the Euclidean distance between solution i and solution u, x_{ij} stands for the normalized value of the j^{th} objective for solution i, x_{ij} indicates the original value of the j^{th} objective for solution i, and $x_j^{\max}$ and $x_j^{\min}$ are the maximum and minimum values of the j^{th} objective, respectively.

Step 13: Comprehensive knee point evaluation function

$$Score_i = 0.4C_i + 0.3S_i + 0.2R_i + 0.1D_i \tag{36}$$

The weighting coefficients were assigned according to the engineering significance of each evaluation criterion, following the common practice in multiple-criteria decision-making (MCDM) where subjective weighting is adopted when different criteria represent distinct engineering priorities. Specifically, the closeness coefficient C_i, which directly reflects the compromise between conflicting objectives and proximity to the ideal solution, was considered as the primary decision criterion and therefore assigned the highest weight (0.4). The stability indicator S_i, evaluating the robustness of a solution under perturbations, was regarded as the second most important criterion (0.3). In contrast, the rank stability R_i and diversity indicator D_i serve as complementary measures to improve the representativeness and reliability of the selected solution, rather than directly reflecting structural performance, and were therefore assigned relatively lower weights (0.2 and 0.1, respectively). The selected weights reflect the relative engineering importance of the four criteria and were intentionally chosen to prioritize solution quality and robustness over auxiliary indicators, consistent with common practice in engineering MCDM studies [71–73]. It should be noted that there is no universally optimal weighting scheme in MCDM, as the relative importance of different criteria inherently depends on the specific engineering objectives and decision context.

Although the entropy-weighted TOPSIS method can rank Pareto solutions based on their closeness to the ideal solution, it has several limitations. It ignores the stability of the solution under perturbations, the consistency of its ranking within the Pareto front, and the diversity of solutions. Therefore, a composite evaluation metric combining the C_i, S_i, R_i, and D_i, was adopted to robustly select the knee point solution that was both representative and reliable. Using the above methodology, the optimal configuration parameters were determined to construct the Vorochiral metamaterials for infilling the forefoot and heel regions of the midsole.

2.3. FE analysis and experimental tests

FE simulations and experimental tests of the optimized structure were conducted to validate the accuracy of the BPNN-predicted mechanical properties. The boundary conditions and loading parameters described in Section 2.2.2 were employed in the FE simulation, and the same meshing strategy method was adopted. Three specimens of the optimized Vorochiral metamaterial were fabricated using the FDM technique with a Bambu Lab P1S 3D printer, as shown in Fig. 9(a). The printing parameters were consistent with those described in Section 2.2.2. Quasi-static compression tests were performed using the same universal testing machine at a loading speed of 2.0 mm/min, as shown in Fig. 9(b). The specimens were subjected to a total compression displacement of 20.0 mm, and the corresponding force-displacement responses were recorded. A high-resolution camera was positioned in front of the specimens to capture real-time deformation during testing.

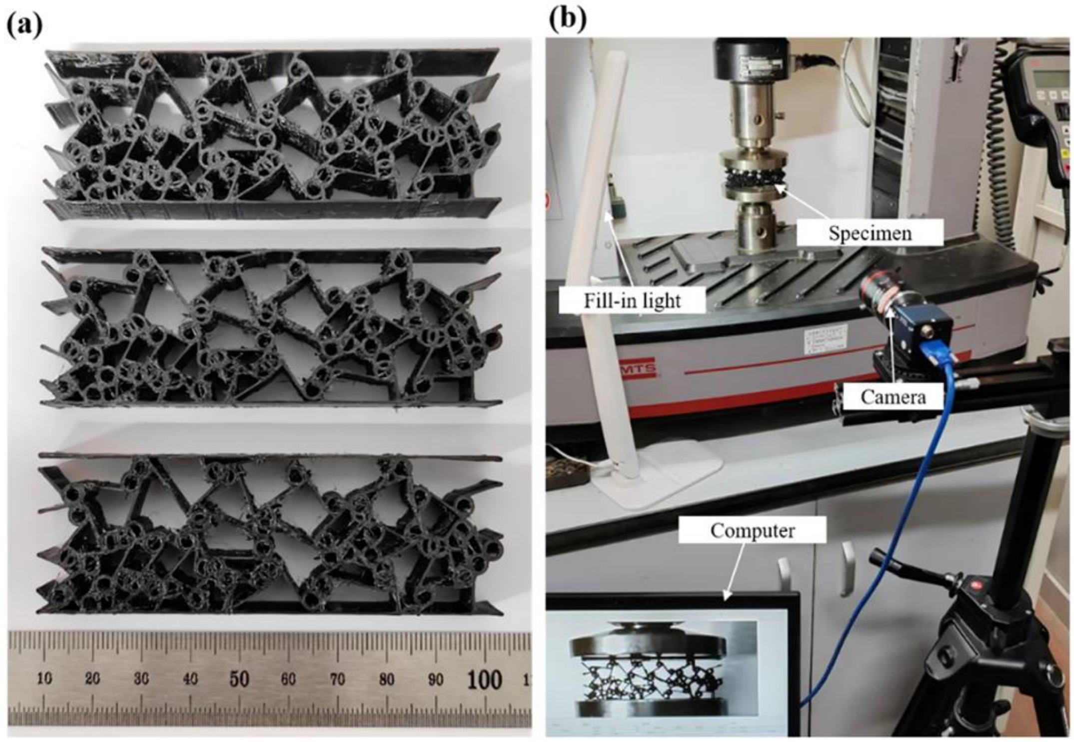

Fig. 9. 3D-printed specimens and experimental testing setup. (a) Fabricated metamaterial specimens. (b) Experimental platform for quasi-static compression testing.

2.4. Measurements of static standing and dynamic gait

Measurements under static standing and dynamic gait conditions were conducted to evaluate the performance of the Vorochiral midsole. The Vorochiral midsole was constructed as shown in Fig. 10(a), with optimized Vorochiral structure infilled into the forefoot and heel regions. The infilling strategy for the midfoot and non-contact regions remained consistent with the lower layer of the optimized structure. The higher density of seed points in these two sections enhanced the stability of the midsole. To provide representative benchmark designs, three widely adopted lattice architectures, namely the uniform Trichiral, uniform Tetrachiral, and uniform Gyroid structures, were selected for comparison, following the common benchmarking strategy adopted in previous studies [74]. The Trichiral and Tetrachiral structures represent conventional chiral lattices, whereas the Gyroid structure represents a typical TPMS architecture. The nodal circle radii of the trichiral and tetrachiral midsoles were identical to those of the Vorochiral midsole. It is worth noting that to ensure a strictly fair comparison of structural and biomechanical performances, all midsoles evaluated in this study were generated with an identical relative density of approximately 26.5%, and their top and bottom plates were assigned the same thickness.

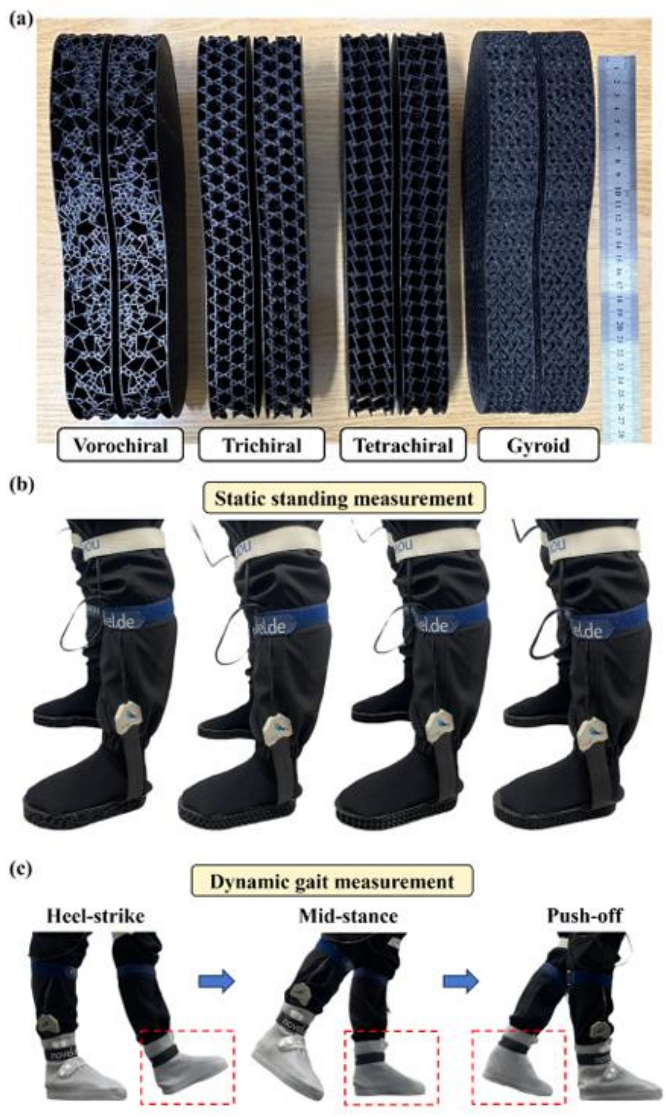

Fig. 10. Midsoles and measurements setups for static standing and gait analysis. (a) Four midsoles with Vorochiral, trichiral, tetrachiral, and Gyroid structures. (b) Static standing measurement setup. (c) Dynamic gait measurement setup.

These midsoles were also fabricated using the FDM 3D printer with TPU 95 A HF, with printing parameters consistent with those described in Section 2.2.2. All specimens were printed under identical processing conditions to ensure consistency among different midsole designs. Owing to its continuous ligament-based architecture without enclosed internal cavities, the proposed Vorochiral metamaterial can be directly fabricated using commercially available FDM technology without requiring specialized manufacturing processes. After fabrication, the support structures were manually removed, and the printed midsoles were cleaned prior to plantar pressure measurements.

Standing is one of the most fundamental human activities. During standing, the pressure distribution between the plantar surface and the support surface reflects physiological, structural, and functional characteristics of the foot, lower limbs, and the entire body. Therefore, feedback on plantar pressure during standing holds significant practical implications for midsole design. To evaluate the performance of the 3D- printed midsoles under static conditions, plantar pressure data were collected through biomechanical testing. The Pedar-X pressure measurement system was used, with sensors placed on the upper surface of the midsole and straps secured around the lower leg. Before each test, the pressure measurement system was calibrated according to the manufacturer's instructions. Four healthy male participants, as shown in Table 2, stood statically on the instrumented midsoles, as shown in Fig. 10(b), and their plantar pressure distributions were recorded. Additionally, subject A was tested under barefoot conditions on the ground, as described in Section 2.1. Four healthy male participants (subjects A-D) were recruited for the plantar pressure evaluation. Each participant completed five measurements for each midsole configuration, standing for 30 s during each measurement.

Table 2
Subjects for measurements of static standing and dynamic gait.

Subject	Weight (kg)	Height (cm)	Foot length (mm)
A	78.9	178.6	253.5
B	65.8	173.7	252.6
C	89.6	174.5	253.8
D	71.4	172.3	251.3

Note: All participants were healthy males aged 23–28 years, with no history of lower-limb injury diseases within the past year.

To evaluate the statistical significance of plantar pressure and con tact area while controlling for potential intra-subject correlations arising from repeated measurements, a linear mixed-effects model (LMM) was conducted using IBM SPSS Statistics (v26, IBM Inc., New York, USA). Midsole design was treated as a fixed factor, and a random intercept grouped by subject was incorporated to account for individual baseline variability. Pairwise comparisons among different cellular structures were adjusted using the Bonferroni method, with the significance level set at $p < 0.05$.

Walking is the most fundamental form of human locomotion. The analysis and assessment of plantar pressure during walking are of considerable importance for clinical diagnosis, evaluation of disease severity, and assessment of postoperative outcomes. Although walking appears simple, it consists of a series of complex coordinated movements. In general, walking is defined as a sequence of consecutive gait cycles, where a gait cycle refers to the interval between two successive heel strikes of the same foot. The Pedar-X pressure measurement system was employed to provide objective, detailed, and quantitative data on plantar pressure changes during walking across different midsole configurations, as shown in Fig. 10(c). During data acquisition, four subjects walked naturally at a self-selected pace while wearing midsoles fitted with shoe covers. Plantar pressure distributions were recorded in real time, capturing pressure variations across the entire plantar surface. A gait cycle consists of a stance phase and a swing phase. The stance phase corresponds to the period during which the single foot is in contact with the ground, accounting for approximately 60% of the gait cycle, while the swing phase comprises for the remaining 40%. In this study, the stance phase of a single step was further divided into three stages, including heel-strike, mid-stance, and push-off, as illustrated in Fig. 10 (c). For each midsole configuration, five measurements were completed in each participant, who walked for 30 s during each measurement.

The studies involving humans were approved and reviewed by the Ethics Committee of Central Hospital of Dalian University of Technology and granted exemption from full ethics review procedures under the relevant Judgement's reference number No. 2023–077–15. The studies were conducted in accordance with the local legislation and institutional requirements. The participants provided their written informed consent to participate in this study.

3. Results and discussion

This section presents a systematic analysis and discussion of the optimization results, FE simulations, mechanical experiments, and measurements under static standing and dynamic gait conditions.

3.1. Data analysis

The initial dataset was generated using OLHS and FE simulations, as detailed in Supplementary table 1. The dataset comprised 50 samples. To improve the prediction accuracy of the BPNN model, a data augmentation approach based on VAE was employed to expand the dataset. To evaluate the validity of the augmented dataset, the Pearson correlation coefficient and t-distributed stochastic neighbor embedding (t-SNE) were utilized.

Pearson correlation coefficient analysis was performed on the augmented dataset to assess variable relationships and support the development of a robust BPNN model. Seven variables, including input design parameters and output mechanical properties, were analyzed in this study. The Pearson correlation coefficient ranges from -1.0 – 1.0， where values closer to 1.0 indicate stronger positive correlation, the values closer to –1.0 indicate stronger negative correlation. Values of 1.0 and -1.0 correspond to perfect positive and perfect negative correlations, respectively. The correlation heatmap is shown in Fig. 11(a). The results indicated that the input variables were largely independent, as reflected by correlation coefficients close to zero. A weak negative correlation was observed between *Ir* and both mechanical performance indicators, whereas n exhibited a weak positive correlation with these indicators. The parameter *r* showed a weak negative correlation with *E* but no discernible correlation with *SEA*. In contrast, *t* demonstrated a weak positive correlation with *SEA* and a strong positive correlation with *E*. Additionally, *g* exhibited a weak negative correlation with both mechanical properties. Notably, a strong positive correlation was observed between *E* and *SEA*, highlighting the inherent coupling between stiffness and energy absorption. This relationship justifies the need for multi-objective optimization. Overall, these findings were consistent with expected physical behavior and provided a sound basis for training a robust BPNN model.

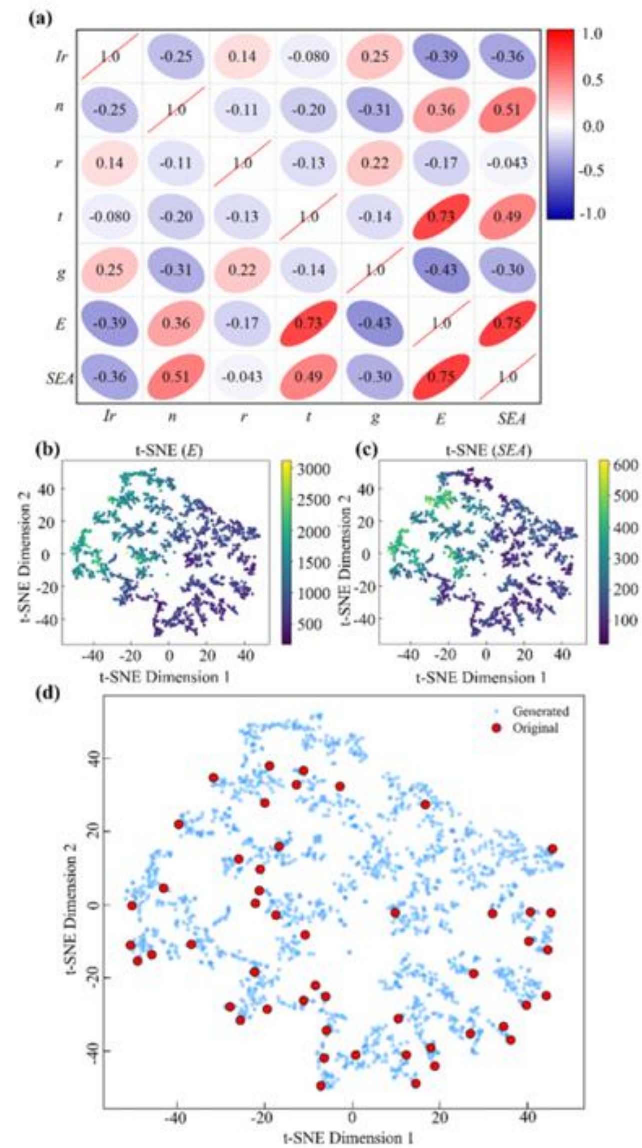

Fig. 11. Data analysis results. (a) Pearson correlation coefficient heatmap. (b) t-SNE visualization of E. (c) t-SNE visualization of SEA. (d) t-SNE visualization of comparison between original and generated data.

To evaluate the fidelity and distribution of the VAE-augmented dataset, t-SNE was employed to project the high-dimensional design space onto a 2D manifold. As illustrated in Figs. 11(b) and 11(c), the augmented data exhibited clear global continuity and local clustering, effectively preserving the underlying physical correlations inherent in the original dataset. Notably, the color-mapped distributions of E and SEA displayed smooth gradient transitions across the latent space. This observation indicates that the VAE successfully captured the complex non-linear mapping between structural design parameters and their corresponding mechanical responses. The absence of significant noise or overlapping disparate target values in the local neighborhoods indicated that the generated data maintained high deterministic consistency. To further verify the fidelity of the VAE-generated samples, both qualitative and quantitative validations were performed. As shown in Fig. 11(d), the t-SNE visualization of the original and generated datasets based on the five design variables is presented, showing substantial overlap between the two datasets without obvious distributional shifts or isolated clusters. Additionally, the statistical characteristics of the five design variables are compared, as shown in Table 3. The generated samples exhibit comparable means and standard deviation (SD) to those of the original dataset while remaining entirely within the predefined design-variable ranges. No physically invalid configurations were observed, indicating that the VAE effectively enriches the sample density without introducing unrealistic samples. Consequently, the augmented dataset provided a robust and comprehensive representation of the design space, ensuring a high-quality data foundation for subsequent BPNN training, thereby enhancing model generalization and predictive accuracy.

Table 3
Statistical distribution comparison of design variables between the original dataset and the VAE-augmented dataset.

Variable	Original Mean	Generated Mean	Original SD	Generated SD	Original Range	Generated Range
Irregularity (*Ir*)	0.600	0.658	0.238	0.220	0.20–1.00	0.206–0.999
Number of seed points (*n*)	14.996	13.040	2.975	2.737	10.0–20.0	10.001–19.931
Nodal circle radius (*r*, mm)	1.750	1.769	0.149	0.136	1.50–2.00	1.503–2.000
Wall thickness (*t*, mm)	0.750	0.825	0.149	0.136	0.50–1.00	0.500–1.000
Gradient factor (*g*)	0.400	0.414	0.119	0.109	0.20–0.60	0.200–0.599

3.2. Predictive performance of BPNN

The predictive performance of the BPNN model is critical for multi- objective inverse optimization design, as an accurate surrogate model can significantly enhance the efficiency and reliability of the inverse design process. Therefore, optimizing the hyperparameters of the BPNN model is essential to achieve high predictive accuracy. The MSE was used as the evaluation metric to compare different BPNN architectures, as illustrated in Fig. 12(a). The number of hidden layers was varied from one to four, with 6, 8, or 10 neurons in each layer. Among the tested configurations, the BPNN model with three hidden layers and 10 neurons per layer achieved the lowest MSE, indicating the optimal architecture for this study.

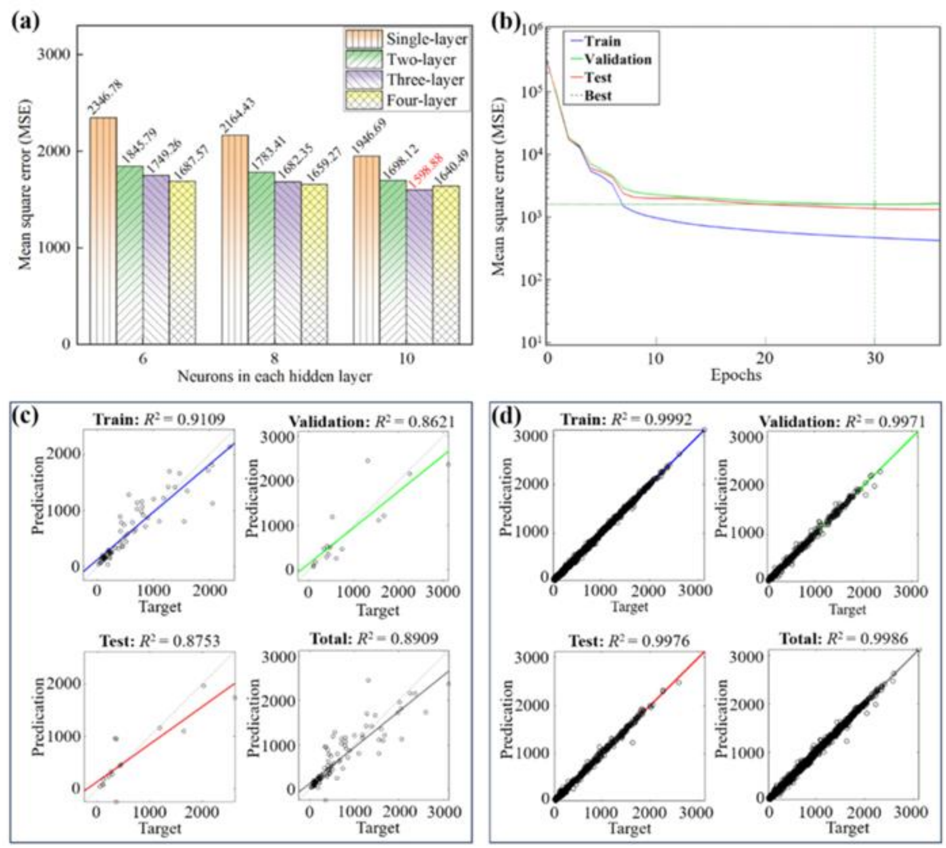

Fig. 12. Sensitivity analysis, convergence behavior, and regression analysis of BPNN. (a) Hyperparameter sensitivity analysis. (b) Convergence behavior. (c) Regression results for the initial datasets. (d) Regression results for augmented datasets. Predicted values are obtained from the BPNN model, while target values are derived from the datasets.

The BPNN model exhibited robust predictive performance, as reflected by the MSE and R values across the training, validation, and test datasets. The convergence behavior of the model is illustrated in Fig. 12 (b). The convergence curves for all datasets were closely aligned, indicating consistent performance and suggesting that the model effectively avoids both overfitting and underfitting. The regression performance of the BPNN model trained on the initial and augmented datasets is presented in Figs. 12(c) and 12(d), respectively. The model trained on the augmented dataset demonstrated significantly improved predictive ac curacy compared with that trained on the initial dataset, confirming the effectiveness of the VAE-based data augmentation approach.

Compared with conventional surrogate models, such as the response surface method (RSM) and Gaussian process regression (GPR, also referred to as the Kriging model), BPNN does not rely on a predefined functional form and exhibits a stronger capability for approximating highly nonlinear relationships. It effectively captures the complex nonlinear mapping between structural design variables and mechanical responses. Furthermore, following VAE-based data augmentation, the training dataset contains approximately 1800 samples. Under such a dataset size, BPNN offers superior scalability and computational efficiency, whereas the computational cost of GPR increases rapidly with the number of training samples. In contrast, the polynomial assumptions inherent in RSM limit its approximation accuracy for highly nonlinear systems. Therefore, BPNN was adopted as the surrogate model to achieve an effective balance between prediction accuracy, computational efficiency, and scalability.

3.3. Optimal configuration

The optimal configuration parameters of the Vorochiral meta material were determined by integrating the BPNN surrogate model with the NSGA-II. To identify a suitable knee point on the Pareto front, a comprehensive decision-making framework based on the entropy weight-TOPSIS method was employed. The resulting Pareto front and the selected knee point are presented in Fig. 13(a). The knee point was identified as the solution achieving the highest score according to the comprehensive evaluation metric, as illustrated in Fig. 13(b). The corresponding optimal configuration parameters are summarized in Table 4. Since the number of seed points n in the middle layer must be an integer, it was rounded to 15. The same rounding procedure was applied to the seed points in the upper and lower layers.

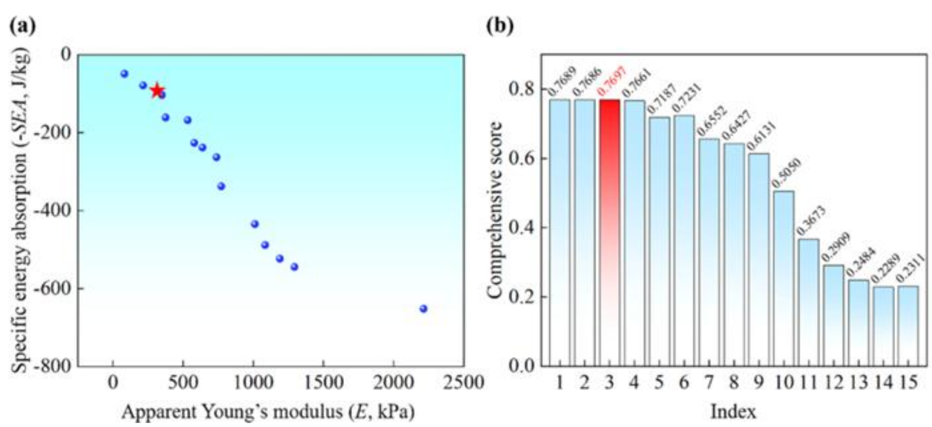

Fig. 13. Pareto front obtained using NSGA-II. (a) Pareto front, where the red star indicates the knee point identified using an entropy weight-TPOSIS-based decision framework. (b) Comprehensive scores of solutions on the Pareto front.

Table 4
Optimal configuration parameters.

Irregularity (Ir)	Number of seed points (n)	Nodal circle radius (r, mm)	Wall thickness (t, mm)	Gradient factor (g)
0.78	15.37	1.82	0.56	0.51

3.4. Experimental validation of FE results and BPNN predictions

The predictive accuracy of the mechanical properties of the optimized Vorochiral metamaterial, as were obtained from the BPNN model, was validated through FE analysis and experimental testing. Based on the determined optimal configuration parameters, the structure was constructed, followed by FE simulations and experimental tests. The FE results were validated against experimental measurements, with particular emphasis on stress-strain responses and deformation behavior. As illustrated in Fig. 14(a), the stress-strain curves from the FE simulations closely matched the experimental results across all three specimens. Minor discrepancies were observed, which can be attributed to differences between the 3D-printed structures and the idealized FE models, particularly in terms of contact conditions, material parameters, and boundary constraints. Additionally, the deformation patterns of the Vorochiral metamaterials showed strong agreement between experimental observations and FE predictions, as presented in Fig. 14(b). The deviations between experimental and FE results remained within an acceptable range, thereby confirming the accuracy and reliability of the FE model. Consequently, the validated FE model can be confidently used to evaluate the mechanical properties of Vorochiral metamaterials.

The BPNN model also demonstrated excellent predictive capability, with the predicted values of E and SEA showing close agreement with both FE results and experimental data. The absolute errors in E among BPNN predictions, FE results, and experimental measurements were all below 6.72%, while those for SEA were all below 3.67%, as shown in Fig. 14(c). These results further confirmed the strong predictive performance of the well-trained BPNN model.

To better elucidate the internal architecture and spatial distribution of the metamaterials within the practical application, side-view photograph of the 3D-printed Vorochiral midsole prototype is presented in Fig. 14(d). Although different geometric parameters are assigned to the forefoot, midfoot, and heel regions to satisfy their respective functional requirements, the entire orthotic midsole is generated as a single continuous Vorochiral lattice. All regions share the same topological architecture and remain geometrically connected without assembling independent lattice blocks. Therefore, continuous load-transfer paths are inherently preserved across regional boundaries. Furthermore, interfacial mismatch and abrupt topological discontinuities, that could otherwise induce local stress concentrations, are avoided. Similar design considerations have also been highlighted in recent studies on architected cellular structures [75,76].

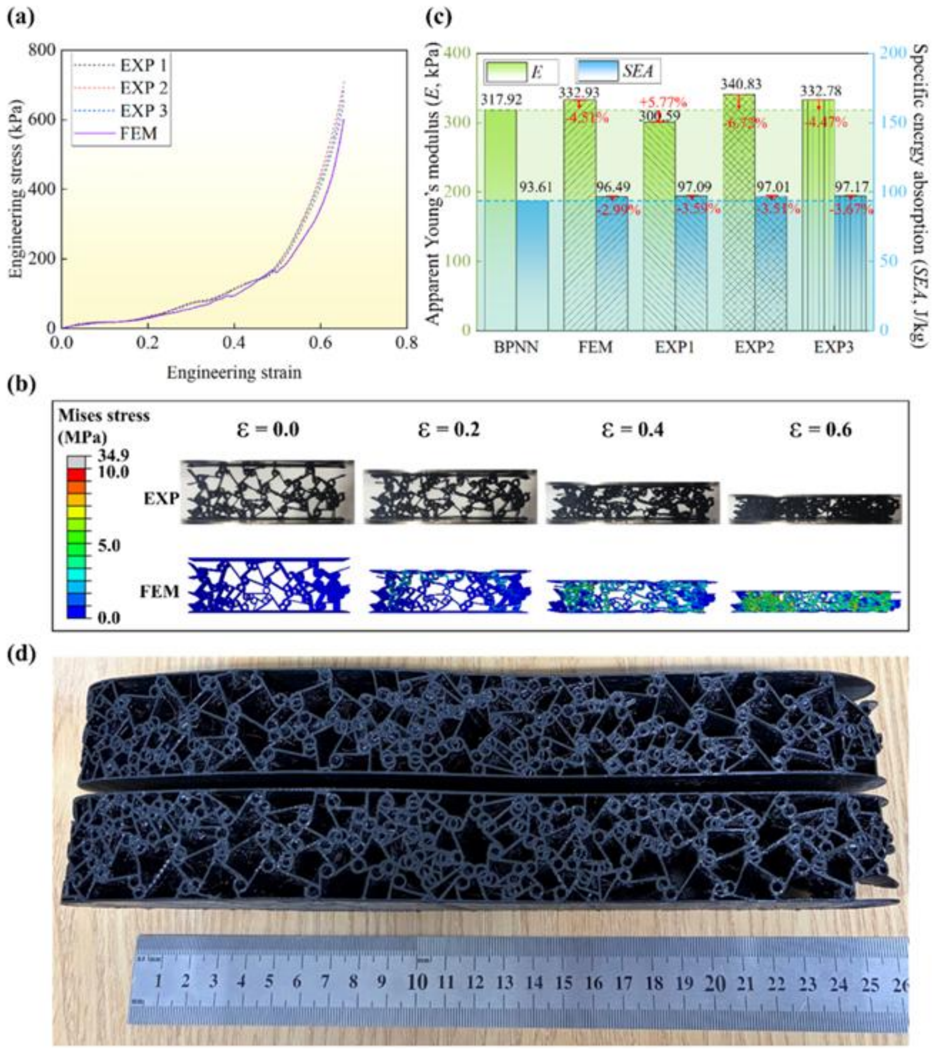

Fig. 14. FE simulation, experimental validation and Vorochiral midsoles. (a) Comparison of stress-strain curves from three experimental tests and FE simulations. (b) Comparison of deformation behavior between experiments and FE simulations. (c) Comparison of apparent Young's modulus (E) and specific energy absorption (SEA) among BPNN predictions, FE

simulations and experimental results. (d) Side-view photograph of the 3D-printed Vorochiral midsole prototype.

3.5. Experimental results of static standing and dynamic gait

To evaluate the performance of the proposed midsole, static standing and dynamic gait experiments were conducted on different midsoles configurations using the Pedar-X pressure measurement system. Under static standing loading conditions, the Vorochiral midsole exhibited significantly lowered peak and mean plantar pressures across all sub jects compared with other midsoles, with the magnitude of reduction varied among individuals. Moreover, the Vorochiral midsole consistently demonstrated a larger contact area than the other three designs. As illustrated in Fig. 15(a)-(d), the results were influenced primarily by the subjects' body weight, while also being affected by foot size and morphology. Across all subjects, the Gyroid midsole consistently showed the highest peak and mean pressures, along with the smallest contact area. The plantar pressure distribution for subject A, shown in Fig. 15(e), followed the same trend. Compared with the Gyroid midsole, the Vorochiral midsole achieved the greatest reduction in peak pressure for subject B, reaching 33.24%. For subject C, it achieved the largest reduction in mean pressure and greatest increase in contact area, reaching 37.94% and 61.17%, respectively. These results indicate that variations in mean pressure and contact area were primarily influenced by body weight, whereas reductions in peak pressure depended not only on body weight but also on foot size and shape. The LMM analysis revealed a statistically significant main effect of the midsole structure on peak plantar pressure, mean plantar pressure, and contact area (all $p < 0.001$ for all pairwise comparisons), successfully verifying the reduction efficiency. Additionally, data are presented as estimated marginal means (EMMeans) ± standard error (SE) derived directly from the LMM, as shown in Table 5. Because the LMM pools the residual variance across groups to control for inter-subject variability, the resulting SE represents the uniform estimation precision of the model for each midsole condition.

Furthermore, as shown in Fig. 15, there is a certain degree of variability in the biomechanical response during the testing. This variability occurs precisely because a generalized "one-size-fits-most" midsole inevitably interacts differently with the unique, dynamic gait patterns and foot morphologies of specific subjects. This inherent variability observed in generalized designs strongly justifies the practical necessity and value of the proposed data-driven inverse design framework. While the current prototype validates the baseline methodology, the proposed framework is intrinsically designed with robust customization capabilities, enabling the automated generation of fully personalized Vorochiral structural configurations based on a specific patient's actual pressure map in future clinical applications.

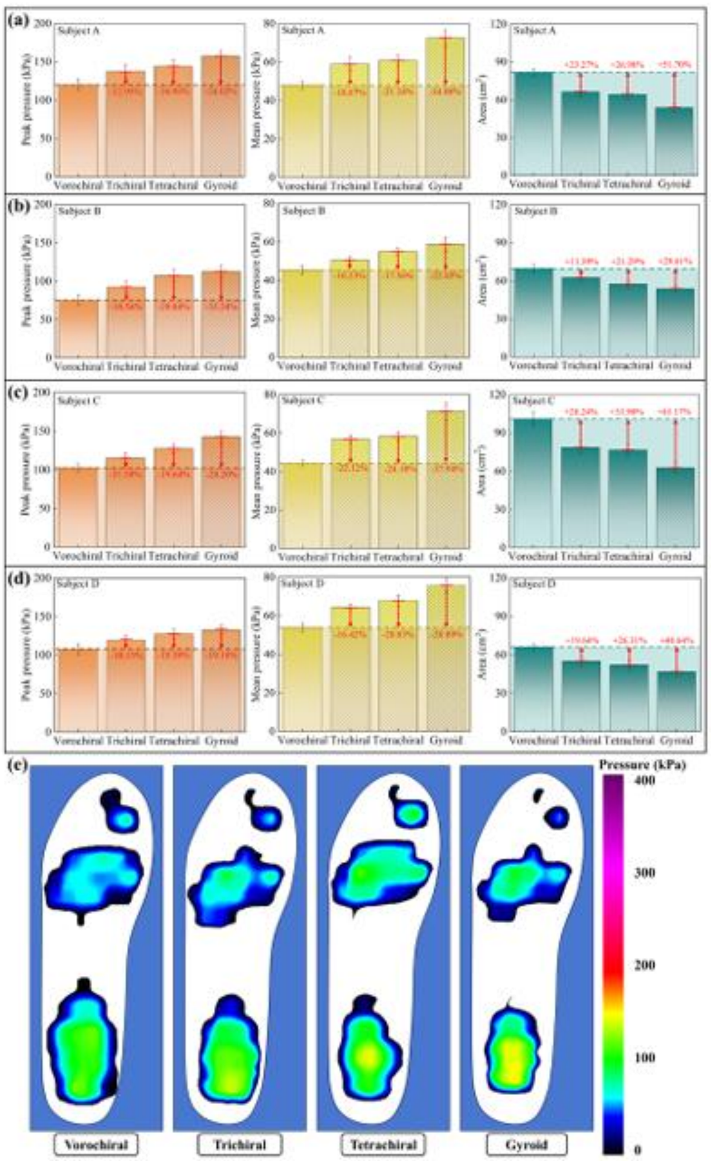

Fig. 15. Peak pressure, mean pressure, and contact area of the plantar region for different midsoles across subjects, along with plantar pressure distributions for subject A. (a-d) Peak pressure, mean pressure, and contact area for subjects A-D, respectively. (e) Plantar pressure distributions of subject A under different midsoles.

Table 5
Quantitative evaluation of plantar pressure and contact area across different cellular structural midsoles based on the linear mixed-effects model (LMM).

Metric	Vorochiral	Trichiral	Tetrachiral	Gyroid	p value
Peak (kPa)	101.32 ±8.90	116.33 ±8.90***	126.71 ±8.90***	136.63 ±8.90***	< 0.001
Mean (kPa)	47.77 ±2.79	57.62 ±2.79***	60.46 ±2.79***	69.52 ±2.79***	< 0.001
Area (cm^2)	79.73 ±5.37	65.77 ±5.37***	62.76 ±5.37***	54.39 ±5.37***	< 0.001

Note: Data are presented as estimated marginal means (EMMeans) ± standard error (SE) derived from the linear mixed-effects model. The overall LMM p-value indicates the main effect of the midsole structure. Asterisks denote significant differences compared to the proposed Vorochiral structure using Bonferroni post-hoc pairwise comparisons. (*$p < 0.05$, **$p < 0.01$, and ***$p < 0.001$.)

Under dynamic gait conditions, the Vorochiral midsole exhibited lower peaks in both peak and mean pressure curves for all subjects compared with the other midsoles, as shown in Fig. 16. Two characteristic pressure peaks occur during gait: one at heel-strike and another at push-off, as shown in Fig. 17. While the overall pressure distribution patterns of the four midsoles were similar, with the heel and forefoot regions serving as the primary load-bearing zones, notable differences are observed in peak and mean pressure magnitudes. When either the heel or forefoot regions is in contact with the ground, Vorochiral midsole consistently exhibits lower peak and mean pressure than other designs.

Overall, the results from both static standing and dynamic gait measurements across multiple subjects demonstrated that the Vorochiral midsole provided superior biomechanical performance compared with midsoles incorporating conventional structures. Specifically, it effectively reduced plantar pressure in the heel and forefoot regions, minimized prolonged localized stress, and alleviates fatigue during walking.

Although the proposed data-driven inverse design framework is demonstrated through the design of customized orthotic midsoles, its methodology is not restricted to this specific application. The present implementation is based on a mechanical database generated under quasi-static compression of TPU Vorochiral metamaterials, with E and SEA selected as the optimization objectives. For other metamaterial design problems involving different materials, loading conditions, or engineering requirements, the proposed framework can be readily extended by reconstructing the training dataset using the corresponding boundary conditions and redefining the optimization objectives, while retaining the same data augmentation, surrogate modeling, and multi- objective optimization strategy.

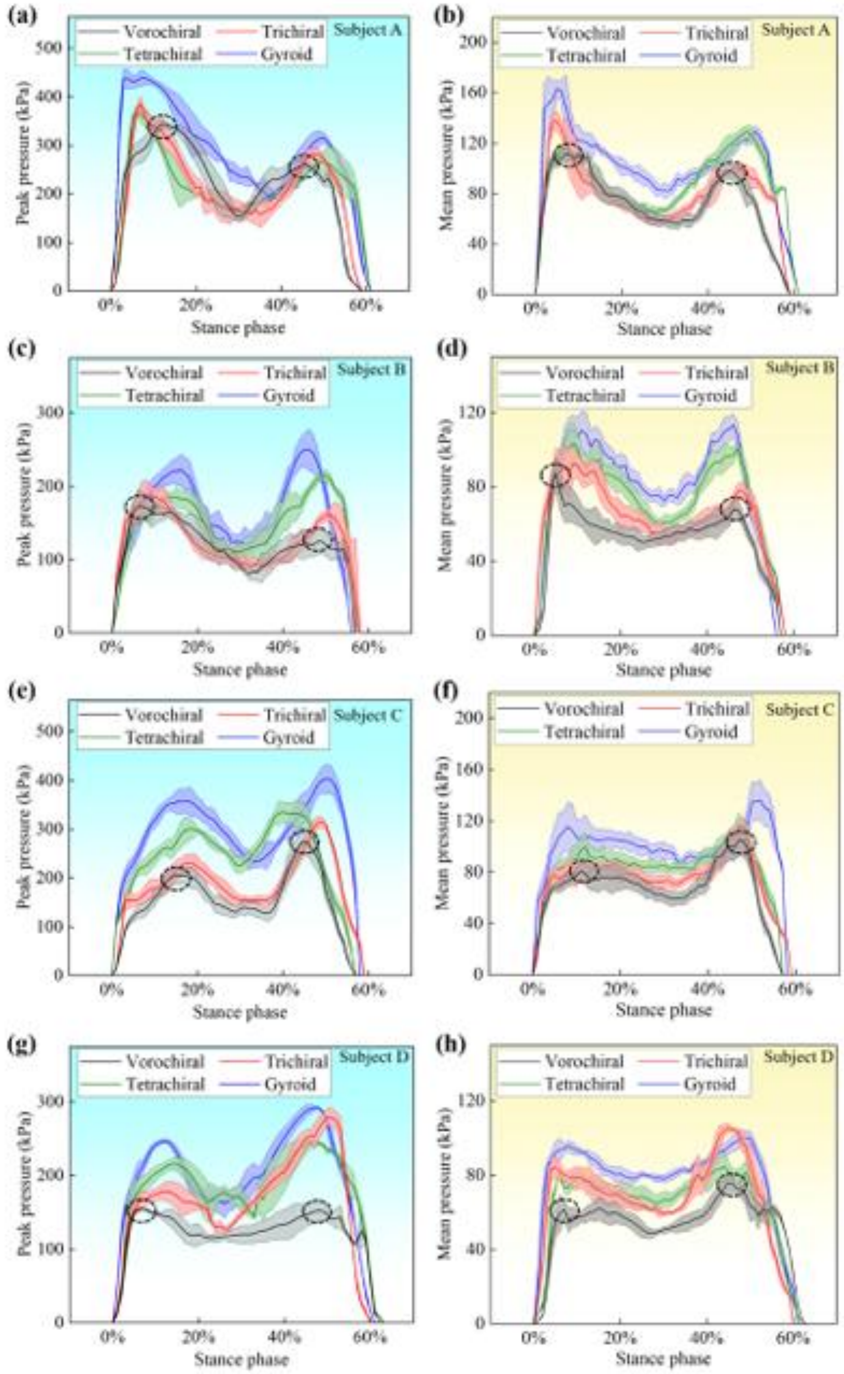

Fig. 16. Peak and mean plantar pressure curves during dynamic gait for different subjects. (a-b) Subject A. (c-d) Subject B. (e-f) Subject C. (g-h) Subject D. The black dashed ovals highlight the peak regions of the pressure curves.

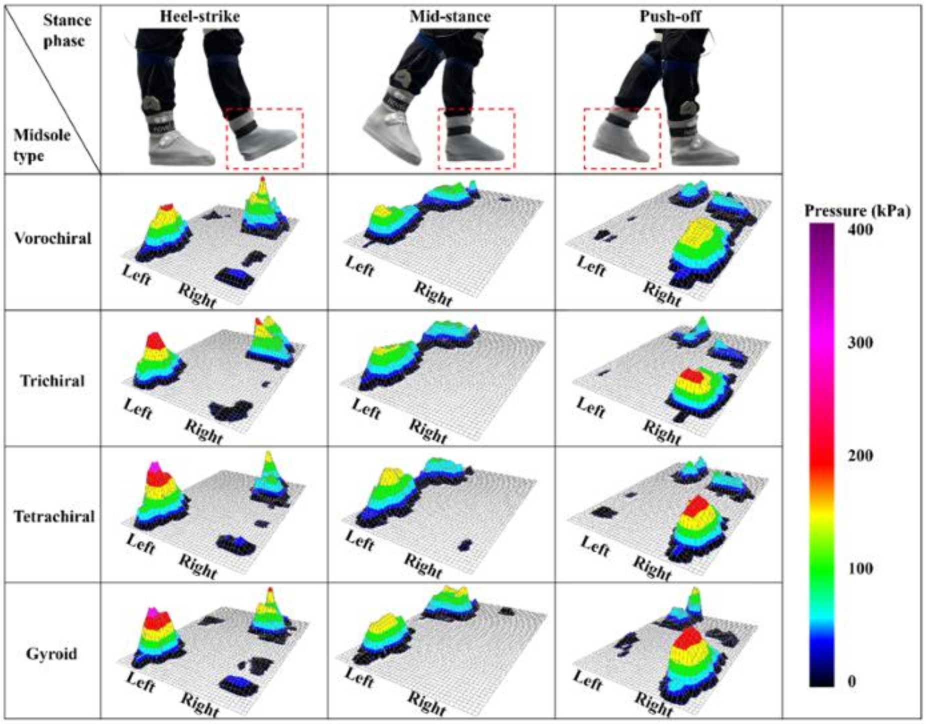

Fig. 17. 3D plantar pressure maps at different gait phases for subject A.

3.6. Limitations of this study

Although the Vorochiral midsole demonstrated excellent performance, several limitations remain in this study. First, the recruited participants were all healthy young male. Further study should include a more diverse cohort in terms of gender, age, and foot health conditions. In particular, customizing and evaluating the midsole design for patients with diabetic foot would enhance the clinical relevance of this work. Furthermore, region-specific design could be implemented, whereby the midsole is partitioned according to individual foot conditions, allowing variations in regional dimensions and tailored infilled structures. Second, the experimental evaluations were limited to static standing and walking. Additional activities, such as stair climbing, uphill walking, and jogging, should be considered to provide a more comprehensive assessment of midsole performance. Third, this study focused on a simplified midsole design, whereas evaluating fully integrated footwear systems would yield more practical insights. Fourth, it should be acknowledged that manufacturing imperfections may introduce deviations in strut dimensions, node positions, and local geometries, which could affect the mechanical response of the fabricated Vorochiral metamaterials. Although small geometric deviations are not expected to fundamentally change the global stochastic topology and dominant deformation mechanisms, their quantitative influence has not been systematically investigated in the present study. In the future work, the sensitivity analysis will be performed to investigate realistic manufacturing tolerances through controlled fabrication and numerical perturbation analyses. Finally, the potential influence of FDM-induced anisotropy on the long-term fatigue performance of thin-walled Vorochiral struts was not explicitly considered in the present study and represents an important direction for future investigation, particularly for repeated-loading applications such as orthotic midsoles.

4. Conclusions

In this study, a data-driven multi-objective inverse optimization design framework was proposed to develop a novel orthotic midsole based on programmable Vorochiral metamaterials. The midsole was partitioned into three primary regions, namely forefoot, midfoot, and heel, according to the plantar pressure distribution. To mitigate high- pressure concentrations in the forefoot and heel regions, an infilling design strategy was implemented. OLHS was employed to construct the initial dataset while reducing computational cost, and a VAE was used to generate an augmented dataset to overcome the problem of small samples. A BPNN was trained as a surrogate model, and multi-objective inverse optimization was performed by integrating the BPNN with the NSGA-II. The optimal configuration parameters were identified from the Pareto front using a comprehensive decision-making framework based on the entropy weight-TOPSIS method. The Vorochiral metamaterial was then constructed based on these parameters, and FE simulations and mechanical experiments were conducted to validate the predictive ac curacy of the BPNN model. Static standing and dynamic gait experiments were further performed to evaluate the biomechanical performance of the designed midsole. Compared with midsoles incorporating conventional structures, the Vorochiral midsole exhibited significantly lower peak and mean plantar pressures during both static standing and walking conditions.

In summary, the principal methodological contribution of this work is the development of a unified data-driven inverse design framework, seamlessly integrating VAE-based data augmentation, BPNN surrogate modeling, multi-objective optimization, and an extended entropy- weight TOPSIS decision strategy, to successfully engineer high- performance Vorochiral midsoles. The optimized midsole demonstrated superior plantar pressure redistribution performance and strong potential for personalized biomechanical intervention in individuals at risk of diabetic foot complications. Furthermore, the proposed framework establishes a versatile and generalizable paradigm for the inverse design and performance modulation of architected meta materials, facilitating customized engineering design and broader applications across diverse engineering domains.

Declaration of Competing Interest

The authors declare that they have no known competing financial interests or personal relationships that could have appeared to influence the work reported in this paper.

Acknowledgements

This work was supported by the National Natural Science Foundation of China (grant number 12572376, W2521087), National Key R&D Program of China (grant number 2024YFE0213500), the Fundamental Research Funds for the Central Universities (grant number DUT25YG245), the State Key Laboratory of Structural Analysis, Optimization and CAE Software for Industrial Equipment (grant number GZ25110), and the China Scholarship Council (grant number 202506060146). Thanks to Prof. Pankaj Pankaj from Edinburgh University for fruitful discussion.

Appendix A. Supporting information

Supplementary data associated with this article can be found in the online version at doi:10.1016/j.tws.2026.115667.

Data availability

Data will be made available on request.

References

[1] Y. Ren, H. Wang, X. Song, Y. Wu, Y. Lyu, W. Zeng, Advancements in diabetic foot insoles: a comprehensive review of design, manufacturing, and performance evaluation, Front. Bioeng. Biotechnol. 12 (2024) 1394758, https://doi.org/10.3389/fbioe.2024.1394758.

[2] E.L. Feldman, B.C. Callaghan, R. Pop-Busui, D.W. Zochodne, D.E. Wright, D. L. Bennett, V. Bril, J.W. Russell, V. Viswanathan, Diabetic neuropathy, Nat. Rev. Dis. Prim. 5 (2019) 41, https://doi.org/10.1038/s41572-019-0092-1.

[3] J.M. Forbes, M.E. Cooper, Mechanisms of diabetic complications, Physiol. Rev. 93 (2013) 137–188, https://doi.org/10.1152/physrev.00045.2011.

[4] A.I. Vinik, M.T. Holland, J.M.L. Beau, F.J. Liuzzi, K.B. Stansberry, L.B. Colen, Diabetic neuropathies, Diabetes Care 15 (1992) 1926–1975, https://doi.org/10.2337/diacare.15.12.1926.

[5] M.P. Khanolkar, S.C. Bain, J.W. Stephens, The diabetic foot, QJM 101 (2008) 685–695, https://doi.org/10.1093/qjmed/hcn027.

[6] W.J. Jeffcoate, K.G. Harding, Diabetic foot ulcers, Lancet 361 (2003) 1545–1551, https://doi.org/10.1016/S0140-6736(03)13169-8.

[7] P.R. Cavanagh, B.A. Lipsky, A.W. Bradbury, G. Botek, Treatment for diabetic foot ulcers, Lancet 366 (2005) 1725–1735, https://doi.org/10.1016/S0140-6736(05)67699-4.

[8] E.J. Boyko, J.H. Ahroni, V. Stensel, R.C. Forsberg, D.R. Davignon, D.G. Smith, A prospective study of risk factors for diabetic foot ulcer. The Seattle Diabetic Foot Study, Diabetes Care 22 (1999) 1036–1042, https://doi.org/10.2337/diacare.22.7.1036.

[9] J. Kalish, A. Hamdan, Management of diabetic foot problems, J. Vasc. Surg. 51 (2010) 476–486, https://doi.org/10.1016/j.jvs.2009.08.043.

[10] B.A. Lipsky, A.R. Berendt, H.G. Deery, J.M. Embil, W.S. Joseph, A.W. Karchmer, J. L. LeFrock, D.P. Lew, J.T. Mader, C. Norden, J.S. Tan, Diagnosis and treatment of diabetic foot infections, Plast. Reconstr. Surg. 117 (2006) 212S, https://doi.org/10.1097/01.prs.0000222737.09322.77.

[11] J.Z.M. Lim, N.S.L. Ng, C. Thomas, Prevention and treatment of diabetic foot ulcers, J. R. Soc. Med. 110 (2017) 104–109, https://doi.org/10.1177/0141076816688346.

[12] D.F. Bandyk, The diabetic foot: Pathophysiology, evaluation, and treatment, Semin. Vasc. Surg. 31 (2018) 43–48, https://doi.org/10.1053/j.semvascsurg.2019.02.001.

[13] A.J. Boulton, L. Vileikyte, G. Ragnarson-Tennvall, J. Apelqvist, The global burden of diabetic foot disease, Lancet 366 (2005) 1719–1724, https://doi.org/10.1016/S0140-6736(05)67698-2.

[14] N.C. Schaper, J.J. van Netten, J. Apelqvist, S.A. Bus, R.J. Hinchliffe, B.A. Lipsky, I. E. Board, Practical guidelines on the prevention and management of diabetic foot disease (IWGDF 2019 update), Diabetes Metab. Res. Rev. 36 (2020) e3266, https://doi.org/10.1002/dmrr.3266.

[15] K. McDermott, M. Fang, A.J.M. Boulton, E. Selvin, C.W. Hicks, Etiology, epidemiology, and disparities in the burden of diabetic foot ulcers, Diabetes Care 46 (2022) 209–221, https://doi.org/10.2337/dci22-0043.

[16] D. Kosaji, M.I. Awad, R. Katmah, H.F. Jelinek, M.F. Domingues, M. Baguneid, A. Alanazi, K. Khalaf, Diabetic foot prevention, assessment, and management using innovative smart wearable technology: a systematic review, J. Neuroeng. Rehabil. 22 (2025) 168, https://doi.org/10.1186/s12984-025-01695-9.

[17] H. Cheng, B. Liu, M. Liu, W. Cao, Design of three-dimensional Voronoi strut midsoles driven by plantar pressure distribution, J. Comput. Des. Eng. 9 (2022) 1410–1429, https://doi.org/10.1093/jcde/qwac060.

[18] R. Zhang, L. Zhao, Q. Kong, G. Yu, H. Yu, Multi-objective design and optimization of high cushioning bionic shoe midsole under limited thickness of forefoot, Compos. Struct. 324 (2023) 117560, https://doi.org/10.1016/j.compstruct.2023.117560.

[19] D. Cracknell, M. Battley, J. Fernandez, M. Amirpour, The mechanical response of polymeric gyroid structures in an optimised orthotic insole, Biomech. Model. Mechanobiol. 24 (2025) 311–329, https://doi.org/10.1007/s10237-024-01912-9.

[20] Y. Sun, Q. Zhou, W. Niu, S. Zhang, K.-L. Yick, B. Gu, W. Xu, 3D printed sports shoe Midsoles: Enhancing comfort and performance through finite element analysis of negative Poisson's ratio structures, Mater. Des. 245 (2024) 113292, https://doi.org/10.1016/j.matdes.2024.113292.

[21] A.M. Ab Rashid, M.H. Ramlee, H.S. Gan, M. Rafiq Abdul Kadir, Effects of badminton insole design on stress distribution, displacement and bone rotation of ankle joint during single-leg landing: a finite element analysis, Sports Biomech. 23 (2024) 3052–3073, https://doi.org/10.1080/14763141.2022.2086168.

[22] M. Kang, H. Choi, K. Park, S. Pyo, Additively manufactured 3D auxetic metamaterials for structurally guided capacitive and resistive tactile sensing, Adv. Funct. Mater. 35 (2025) e09704, https://doi.org/10.1002/adfm.202509704.

[23] D. Cracknell, M. Battley, J. Fernandez, M. Amirpour, Static and dynamic optimisation of fluid-filled responsive orthotic insoles, Biomech. Model. Mechanobiol. 24 (2025) 713–741, https://doi.org/10.1007/s10237-025-01935-w.

[24] M. Alam, T.H. Kwok, Multidisciplinary optimization of shoe midsole structures using swarm intelligence, Struct. Multidiscip. Optim. 67 (2024) 134, https://doi.org/10.1007/s00158-024-03845-4.

[25] J. Shuang, A. Haron, D. Crosby, M. Mansoubi, G.J. Massey, C. Lin, F.L. Bowling, N. D. Reeves, H. Dawes, G. Cooper, A. Weightman, An active insole to reduce plantar pressure loading: Using predictive finite element driven soft hydraulic actuators to minimize plantar pressure and the pressure time integral for diabetic foot ulceration risk management, IEEE Trans. Biomed. Eng. 72 (2025) 2882–2892, https://doi.org/10.1109/TBME.2025.3554888.

[26] I. Jung, S. Lee, Characterization of 3D printed re-entrant midsole structure with various infill density and print direction, Sci. Rep. 15 (2025) 43719, https://doi.org/10.1038/s41598-025-27421-y.

[27] K. Kim, H. Kim, W. Hwang, Y. Choi, K. Kim, J. Ahn, H. Lee, A multidisciplinary review on footwear 3D printing: From biomechanics to therapeutics, Int. J. Bioprinting 11 (2025) 98–121, https://doi.org/10.36922/IJB025210204.

[28] M.Y. Khalid, Z.U. Arif, A. Tariq, M. Hossain, R. Umer, M. Bodaghi, 3D printing of active mechanical metamaterials: A critical review, Mater. Des. 246 (2024) 113305, https://doi.org/10.1016/j.matdes.2024.113305.

[29] H. Wang, Y. Lyu, S. Bosiakov, H. Zhu, Y. Ren, A review on the mechanical metamaterials and their applications in the field of biomedical engineering, Front. Mater. 10 (2023) 1273961, https://doi.org/10.3389/fmats.2023.1273961.

[30] P. Jiao, J. Mueller, J.R. Raney, X. (Rayne) Zheng, A.H. Alavi, Mechanical metamaterials and beyond, Nat. Commun. 14 (2023), https://doi.org/10.1038/s41467-023-41679-8.

[31] W.W.S. Ma, H. Yang, Y. Zhao, X. Li, J. Ding, S. Qu, Q. Liu, Z. Hu, R. Li, Q. Tao, H. Mo, W. Zhai, X. Song, Multi-physical lattice metamaterials enabled by additive manufacturing: Design principles, interaction mechanisms, and multifunctional applications, Adv. Sci. 12 (2025), https://doi.org/10.1002/advs.202405835.

[32] K. Bertoldi, V. Vitelli, J. Christensen, M. Van Hecke, Flexible mechanical metamaterials, Nat. Rev. Mater. 2 (2017), https://doi.org/10.1038/natrevmats.2017.66.

[33] A.A. Zadpoor, Mechanical meta-materials, Mater. Horiz. 3 (2016) 371–381, https://doi.org/10.1039/c6mh00065g.

34] P. Sinha, T. Mukhopadhyay, Programmable multi-physical mechanics of mechanical metamaterials, Mater. Sci. Eng. R. Rep. 155 (2023) 100745, https://doi.org/10.1016/j.mser.2023.100745.

[35] M. Pishvar, R.L. Harne, Foundations for soft, smart matter by active mechanical metamaterials, Adv. Sci. 7 (2020), https://doi.org/10.1002/advs.202001384.

[36] L. Zhang, S. Yan, W. Liu, Y. Liu, W. Cai, Z. Zhang, J. Zhou, Mechanical metamaterials with negative Poisson's ratio: A review, Eng. Struct. 329 (2025) 119838, https://doi.org/10.1016/j.engstruct.2025.119838.

[37] J. Chen, J. Chen, H. Wang, L. He, B. Huang, S. Dadbakhsh, P. Bartolo, Fabrication and development of mechanical metamaterials via additive manufacturing for biomedical applications: A review, Int. J. Extrem. Manuf. 7 (2024) 012001, https://doi.org/10.1088/2631-7990/ad88e3.

[38] Z. Cai, X. Deng, Recent advances in reinforced honeycomb mechanical metamaterials: a review, Mater. Des. 263 (2026) 115593, https://doi.org/10.1016/j.matdes.2026.115593.

[39] S. Li, W. Zhang, S. Ding, J. Lu, Y.-Q. Ni, A comprehensive review on energy- absorbing mechanical metamaterials: From mechanisms to applications, Compos. Part. B Eng. 311 (2026) 113222, https://doi.org/10.1016/j.compositesb.2025.113222.

[40] J. Gu, W. Zhao, C. Zeng, L. Liu, J. Leng, Y. Liu, Construction of mechanical metamaterials and their extraordinary functions, Compos. Struct. 356 (2025) 118872, https://doi.org/10.1016/j.compstruct.2025.118872.

[41] K. Ning, M.-Y. Kwan, K.-L. Yick, Design, mechanical evaluation, and wear trial of 3D printed insole for plantar off-loading in older adults with diabetes, Gait Posture 125 (2026) 110102, https://doi.org/10.1016/j.gaitpost.2026.110102.

[42] H. Wang, M.R.A. Kadir, H. Zhu, Y. Lyu, A novel random chiral metamaterial with multi-step plateau: Vorochiral metamaterial, Int. J. Mech. Sci. 315 (2026) 111438, https://doi.org/10.1016/j.ijmecsci.2026.111438.

[43] F. Haris, Y.-K. Jan, B.-Y. Liau, C.-W. Hsieh, W.-C. Shen, C.-C. Tai, Y.-H. Shih, C.- W. Lung, Plantar pressure gradient and pressure gradient angle are affected by inner pressure of air insole, Front. Bioeng. Biotechnol. 12 (2024) 1353888, https://doi.org/10.3389/fbioe.2024.1353888.

[44] P.E. Chatzistergos, A. Gatt, C. Formosa, K. Farrugia, N. Chockalingam, Optimised cushioning in diabetic footwear can significantly enhance their capacity to reduce plantar pressure, Gait Posture 79 (2020) 244–250, https://doi.org/10.1016/j.gaitpost.2020.05.009.

[45] G. Melia, P. Siegkas, J. Levick, C. Apps, Insoles of uniform softer material reduced plantar pressure compared to dual-material insoles during regular and loaded gait, Appl. Ergon. 91 (2021) 103298, https://doi.org/10.1016/j.apergo.2020.103298.
[46] Y. Sterman, D. Solav, N. Rosen, E. Saffuri, L. Shmilov Zaritsky, Custom orthotic insoles with gradual variable stiffness using 3D printed spacer technique, Virtual Phys. Prototyp. 19 (2024) e2336151, https://doi.org/10.1080/17452759.2024.2336151.
[47] H.S. Abdullahi, S. Gao, A novel multi-cell square tubal structure based on Voronoi tessellation for enhanced crashworthiness, Thin-Walled Struct. 150 (2020) 106690, https://doi.org/10.1016/j.tws.2020.106690.
[48] R. Hou, P. Dong, J. Hu, Z. Gong, S. Sadeghzade, J. Cao, H. Yuan, An optimized lozenge-chiral auxetic metamaterial with tunable auxeticity and stiffness, Mater. Des. 237 (2024) 112530, https://doi.org/10.1016/j.matdes.2023.112530.
[49] Y. Yang, L. Zhang, S. Zhang, S. Ling, L. Wu, W. Zou, Bio-inspired graded lattices for enhanced energy absorption, Int. J. Mech. Sci. 312 (2026) 111217, https://doi.org/10.1016/j.ijmecsci.2026.111217.
[50] X.-C. Zhang, Z.-Y. Song, Y.-N. Li, L.-J. Xiao, Z. Xu, L.-X. Rao, T.-J. Ci, X.-L. Hui, Generative inverse design of metamaterials with customized stress-strain response, Int. J. Mech. Sci. 306 (2025) 110875, https://doi.org/10.1016/j.ijmecsci.2025.110875.
[51] S. Zou, H. Gong, Y. Wang, L. Wang, Y. Fan, Study on design and impact energy absorption of network Voronoi lattice structure with directional regulation of load transfer paths, Thin-Walled Struct. 218 (2026) 113920, https://doi.org/10.1016/j.tws.2025.113920.
[52] H. Wang, Y. Lyu, J. Jiang, H. Zhu, Data-driven inverse design of novel spinodoid bone scaffolds with highly matched mechanical properties in three orthogonal directions, Mater. Des. 251 (2025) 113697, https://doi.org/10.1016/j.matdes.2025.113697.
[53] R. Yousefi-Nooraie, N. Razavi, F. Berto, M. Guagliano, S. Bagherifard, Inverse multi-objective design of three-dimensional plate-based heterogeneous mechanical metamaterials, Int. J. Mech. Sci. 312 (2026) 111253, https://doi.org/10.1016/j.ijmecsci.2026.111253.
[54] Z. Zong, Z. Chai, X. Ke, H. Ding, C.F. Guo, Z. Wu, Machine-learning-powered, rapid, accurate, and multi-target mechanical metamaterials inverse design, Small 21 (2025) 2500634, https://doi.org/10.1002/smll.202500634.

[55] Y. Zhang, M. Chen, Z. Chen, T. Zhao, L. Xi, Y. Huang, Data-driven multi-objective optimization and integrated realization of high-performance lattice structures: design, manufacturing, and experimental validation, Eng. Struct. 345 (2025) 121544, https://doi.org/10.1016/j.engstruct.2025.121544.

[56] M. Shaaban, S. El-Borgi, A. Krishnamoorthy, Inverse design of TPMS lattices with targeted phononic bandgaps using multi-objective Bayesian optimization, Mater. Des. 265 (2026) 115891, https://doi.org/10.1016/j.matdes.2026.115891.

[57] A. Satpati, M. Maurizi, D. Yao, S. Kim, H.F. Wu, E.C. Lee, X. (Rayne) Zheng, Multi-objective automatic discovery of optimized metamaterials for varying velocity impact protection, Mater. Des. 258 (2025) 114657, https://doi.org/10.1016/j.matdes.2025.114657.

[58] Z. Hu, J. Ding, S. Ding, W.W.S. Ma, J.W. Chua, X. Li, W. Zhai, X. Song, Machine learning – enabled inverse design of shell-based lattice metamaterials with optimal sound and energy absorption, Virtual Phys. Prototyp. 19 (2024) e2412198, https://doi.org/10.1080/17452759.2024.2412198.

[59] D. Wu, Z. Xu, E. Wu, Z. Yuan, D. Guo, Z. Zhang, Machine learning-driven customizable mechanical design of diamond plate lattice metamaterials, Int. J. Mech. Sci. 310 (2026) 111140, https://doi.org/10.1016/j.ijmecsci.2025.111140.

[60] H. Ou, S. Johnson, Boosting energy return using 3D printed midsoles designed with compliant constant force mechanisms, J. Mech. Des. 146 (2024) 062001, https://doi.org/10.1115/1.4064164.

[61] C.S. Ha, D. Yao, Z. Xu, C. Liu, H. Liu, D. Elkins, M. Kile, V. Deshpande, Z. Kong, M. Bauchy, X. Zheng, Rapid inverse design of metamaterials based on prescribed mechanical behavior through machine learning, Nat. Commun. 14 (2023) 5765, https://doi.org/10.1038/s41467-023-40854-1.

[62] H.X. Zhu, J.R. Hobdell, A.H. Windle, Effects of cell irregularity on the elastic properties of 2D Voronoi honeycombs, –70, J. Mech. Phys. Solids 49 (2001) 857, https://doi.org/10.1016/S0022-5096(00)00046-6.

[63] H.X. Zhu, S.M. Thorpe, A.H. Windle, The geometrical properties of irregular two-dimensional Voronoi tessellations, Philos. Mag. A 81 (2001) 2765–2783, https://doi.org/10.1080/01418610010032364.

[64] D.E. Rumelhart, G.E. Hinton, R.J. Williams, Learning representations by back- propagating errors, Nature 323 (1986) 533–536, https://doi.org/10.1038/323533a0.

[65] S. Gao, H. Dong, Y. Zhang, Y. Sun, C. Yu, Z. Wang, H. Zhang, Y. Huang, Y. Li, Rapid prediction of effective absorption bandwidth in PEEK/CF additive manufacturing metastructure via interpretable machine learning, J. Mater. Sci. Technol. 239 (2025) 307–319, https://doi.org/10.1016/j.jmst.2025.03.060.

[66] S. Gao, Y. Sun, L. Xi, T. Zhao, Y. Huang, R. He, X. Kang, Y. Li, Recent advances in machine learning-assisted design of additive manufacturing metastructures: a review, Compos. Struct. 372 (2025) 119525, https://doi.org/10.1016/j.compstruct.2025.119525.

[67] K. Deb, A. Pratap, S. Agarwal, T. Meyarivan, A fast and elitist multiobjective genetic algorithm: NSGA-II, IEEE Trans. Evol. Comput. 6 (2002) 182–197, https://doi.org/10.1109/4235.996017.

[68] H. Ma, Y. Zhang, S. Sun, T. Liu, Y. Shan, A comprehensive survey on NSGA-II for multi-objective optimization and applications, Artif. Intell. Rev. 56 (2023) 15217–15270, https://doi.org/10.1007/s10462-023-10526-z.

[69] Y. Wang, L. Hong, Z. Liu, L. Sun, L. Liu, Rheological performance evaluation of activated carbon powder modified asphalt based on TOPSIS method, Case Stud. Constr. Mater. 20 (2024) e02963, https://doi.org/10.1016/j.cscm.2024.e02963.

[70] X. Liu, Y. Yang, J. Jiang, The behavioral TOPSIS based on prospect theory and regret theory, Int. J. Inf. Technol. Decis. Mak. 22 (2023) 1591–1615, https://doi.org/10.1142/S0219622022500778.

[71] T.-C. Wang, H.-D. Lee, Developing a fuzzy TOPSIS approach based on subjective weights and objective weights, Expert. Syst. Appl. 36 (2009) 8980–8985, https://doi.org/10.1016/j.eswa.2008.11.035.

[72] M. Alemi-Ardakani, A.S. Milani, S. Yannacopoulos, G. Shokouhi, On the effect of subjective, objective and combinative weighting in multiple criteria decision making: a case study on impact optimization of composites, Expert. Syst. Appl. 46 (2016) 426–438, https://doi.org/10.1016/j.eswa.2015.11.003.

[73] E. Haktanır, C. Kahraman, Integrated AHP & TOPSIS methodology using intuitionistic Z-numbers: an application on hydrogen storage technology selection, Expert. Syst. Appl. 239 (2024) 122382, https://doi.org/10.1016/j.eswa.2023.122382.

[74] S. Gao, Y. Sun, L. Xi, T. Zhao, Y. Huang, R. He, X. Kang, Y. Li, Microwave absorption optimization via additive manufacturing: process-dependent mechanisms of electromagnetic attenuation, Carbon 245 (2025) 120795, https://doi.org/10.1016/j.carbon.2025.120795.
[75] H. Dong, S. Gao, C. Yu, Z. Wang, Y. Huang, T. Zhao, Y. Li, Enhancing microwave absorption of bio-inspired structure through 3D printed concentric infill pattern, Compos. Part. B Eng. 289 (2025) 111924, https://doi.org/10.1016/j.compositesb.2024.111924.
[76] S. Gao, Y. Huang, R. He, X. Kang, Y. Li, Comprehensive unraveling of CT-derived defect characteristics in fused deposition modeling via machine learning: clustering, classification, regression and process correlation, Compos. Part. Appl. Sci. Manuf. 209 (2026) 109942, https://doi.org/10.1016/j.compositesa.2026.109942.